Supplemental Information

Programming Self-Assembly of DNA Origami Honeycomb 2D Lattices and Plasmonic Metamaterials

Pengfei Wang[1], Stavros Gaitanaros[2],Seungwoo Lee[3], Mark Bathe[2], William M. Shih[4,5,6], Yonggang Ke[1*]

[1]Wallace H. Coulter Department of Biomedical Engineering, Georgia Institute of Technology and Emory University, Atlanta, GA 30322, USA
[2]Department of Biological Engineering, Massachusetts Institute of Technology, Cambridge, MA 02139, USA
[3]SKKU Advanced Institute of Nanotechnology & School of Chemical Engineering, Sungkyunkwan University (SKKU), Suwon, 16419, Republic of Korea
[4]Wyss Institute for Biologically Inspired Engineering, Harvard University, Boston, MA 02115, USA
[5]Department of Cancer Biology, Dana-Farber Cancer Institute, Harvard Medical School, Harvard University, Boston, MA 02115, USA
[6]Department of Biological Chemistry and Molecular Pharmacology, Harvard Medical School, Harvard University, Boston, MA 02115, USA
*Corresponding author: Yonggang Ke (yonggang.ke@emory.edu)

Contents

List of Figures

S1 Summary figure

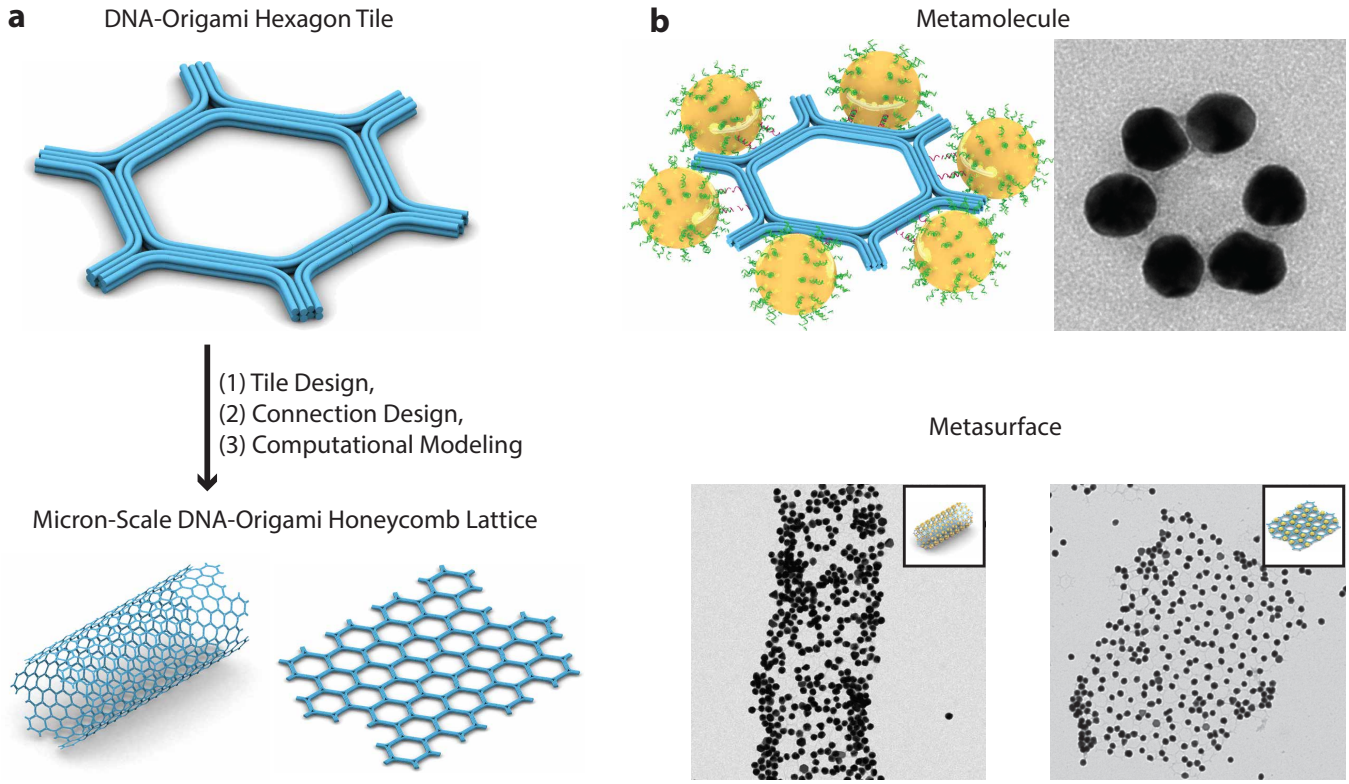

Fig. S1. Self-assembly of DNA-origami hexagon tile and honeycomb lattice (a) and its utilization for fabricating plasmonic metamaterials (b).

S2 Methods and materials

Materials. Short DNA staple strands were purchased from IDT and used as received without purification. M13 Bacteriophage single-stranded DNA (p7560) were used as scaffold for origami construction and produced following a published protocol.[1] AuNPs were purchased from Ted Pella, Inc.

Sample preparation. DNA HTs were deigned using caDNAno. In a typical sample preparation, staples were mixed with single stranded DNA scaffold (p7560, 10 nM) in 10-fold molar excess in folding buffer (5 mM Tris base, 1 mM EDTA, supplement with 14-22 mM $MgCl_2$) with total volume of 50 μL. The mixed solution was slowly cooled down to room temperature (24 °C) in a PCR thermal cycler over 72 hrs in the following protocol: 65 °C for 5 mins, 60 to 24 °C, at 120 mins/°C. For AuNP attachment, HTs, tubes or 2D lattices were assembled first. Purified hexagon tile monomers from agarose gel were incubated with excessive amount of AuNPs for at least 2 hrs at room temperature to form clusters. The corresponding bands for the designated AuNP clusters were extracted from agarose gel for further TEM imaging and UV-Vis absorbance measurements. Assembled tubes or 2D lattices were directly mixed with AuNPs at designated ratio depending on designed patterns of AuNP superlattices, for at least 2 hrs at room temperature. AuNP superlattices were then subject to characterization of TEM imaging and UV-Vis absorbance measurements.

Conjugation of DNA onto AuNPs. 50 mL of colloidal citrated AuNP solution was added with 15 mg of Bis(p-sulfonatophenyl)phenylphosphine dihydrate dipotassium salt (BSPP) and shaked overnight. Then NaCl was added until a colour change of the solution from red to blue was observed. The AuNPs were centrifuged to the bottom at 1,000 rcf for 30 min and the clear supernatant was removed with a pipette. The particles were dissolved in BSPP solution (1 mL, 2.5 mM) followed by addition of 3 mL of methanol. The particles were centrifuged again and re-suspended in 1 mL of BSPP. The concentration of the AuNPs was determined from the optical absorption at a wavelength of 520 nm using a Nanodrop spectrophotometer. For reducing the disulfide bonds of the thiolated ssDNA strands to monothiol, the modified strands were incubated with 100 fold of TCEP (Tris(carboxyethyl) phosphine hydrochloride) for at least 30 mins. AuNPs and thiolated oligonucleotides were mixed in 0.5×TBE buffer at a designated ratio (1: 2000 for 30 nm AuNP). Within a period of 24 hrs, NaCl solution was added to the solution to achieve a final concentration of 300 mM. To remove the unbound thiolated strands, the mixture was spun for 5 min at 12,000 rcf through a 100kDa MWCO centrifugal filter (Amicon Ultra, Millipore) followed by additional 4 spinning steps (5 min, 12,000 rcf) with 400 μL of 0.5 × TBE buffer added to the centrifugal filter before each step. The unbound oligonucleotides should be removed right before adding the AuNPs to the DNA origami structures otherwise newly detached free oligonucleotides will block the hybridization sites of the DNA origami structure.

Gel electrophoresis. Annealed hexagon tile monomers and AuNP clusters were subjected to 1.5 percent native agarose gel electrophoresis for 2 hours (gel prepared in 0.5 × TBE buffer supplemented with 11 mM $MgCl_2$ and 0.005% (v/v) EtBr) in an ice water bath. Then, the target gel bands were excised and placed into a Freeze 'N Squeeze column (Bio-Rad Laboratories, Inc.). The gel pieces were crushed into fine pieces by a microtube pestle in the column, and the column was then centrifuged at 7000 g for 5 minutes. Samples that were extracted through the column were collected for TEM or AFM imaging.

TEM imaging. For imaging, 2.5 μL of annealed sample were adsorbed for 2 minutes onto glow-discharged, carbon-coated TEM grids. The grids were then stained for 10 seconds using a 2% aqueous uranyl formate solution containing 25 mM NaOH. Imaging was performed using a JEOL JEM-1400 TEM operated at 80 kV.

AFM imaging. AFM images were obtained using an SPM Multimode with Digital Instruments Nanoscope V controller (Veeco). 5 μL of purified sample was applied onto the surface of a freshly cleaved mica chip and left for approximately 2 minutes to allow for absorption. 40 μL of 0.5 × TE (10 mM $MgCl_2$) was then added onto the mica surface. The AFM tips used were on the short and thin cantilevers in the SNL-10 silicon nitride cantilever chip (Veeco Probes).

Structure modeling of DNA-origami HTs and lattices. The ground-state 3D solution shapes of DNA-origami HTs and lattices were predicted by CanDo[2–4] using standard geometric and mechanical properties of B-form DNA. Briefly, the procedure starts by parsing the sequence-based representations of a single tile and the topology of larger lattices is constructed algorithmically. The finite element method is then used to find the equilibrium of each structure by minimizing the strain energy while simultaneously satisfying all topological constraints as well as the empirically chosen ground-state geometries of duplexes and four-way junctions. In this framework, DNA duplexes are modeled with 2-node beam elements with a stretching stiffness of 1100 pN, bending stiffness of 230 pN·nm^2 and torsional stiffness of 460 pN·nm^2, where all values correspond to B-form DNA. Four-way junctions are assumed to exist in a single, known ground-state configuration with interhelical distance that is chosen to be 1.85 nm and a rotational stiffness of 135 pN·nm/rad. A zero ground-state angle is assumed between the duplexes at four-way junctions in order to account for the short distance between cross-over positions in the tile designs.

Numerical calculation of AuNP clusters and lattices. The scattering, absorption, and total extinction coefficients of individ-

ual AuNP and AuNP clusters were calculated by numerical simulation, powered by our home-built finite-different, time-domain (FDTD).[5] For the rationalization of UV-VIS absorption measurement result, the scattered and absorbed light from a single AuNP or AuNP clusters/lattices were integrated over all angles. Meanwhile, the FDTD code especially for rationalizing dark-field spectral result was designed to account for the incident angle of a white light source (i.e., 70°) and the collection angle (±70°). In order to integrate the scattering light within such collection angle, near-to-far field transformation was employed.[6] The complex dielectric constants of Au were taken from Johnson and Christy library,[7] while dielectric constants of carbon layer in TEM grid and organic ligand were empirically obtained by ellipsometry. As with previous work,[5] the organic ligand, coated onto AuNP, was assumed to be 1 nm. The whole FDTD computation domain ($1200\times1200\times1200$ nm^3) was uniformly discretized by 2 nm spatial grid along x-,y-, and z-directions. To remove unphysical reflection from the computation domain, perfect matched layer with 200 nm thickness was implemented at each facet of domains. The electric displacement field (black arrow in Fig. 5f) at the frequency of a magnetic dipole mode was calculated by using commercially available FDTD software package (i.e., CST Microwave Studio).

Dark-field spectroscopy. First, the gel-purified buffer solution of AuNP clusters were dispersed onto oxygen plasma-treated TEM grid and dried under nitrogen-gas purging. Particularly, the concentration of AuNP clusters was diluted to be tens of pico molar; this tens of pico molar concentration was optimized to isolate AuNPs clusters on TEM grid with a minimized aggregation. Then, we used a home-built dark-field spectroscopy, in which both spectrometer (IsoPlane SCT 320, Princeton Instrument) and charge-coupled device (CCD) imager (PIXIS 400B, Princeton Instrument) are implemented into the commercially available optical microscope (Nikon Eclipse Ti-E).[5] A polarized white light source, passed through a microscope objective lens (NA = 0.9), was irradiated onto the assembled AuNP clusters; the incident angle was 70 °. The scattered light was selectively collected from the isolated AuNP clusters by using a microscope objective lens (NA = 0.9).[5] Therefore, the collection angle was set by ±70°. This collected scattering light was designed to be passed through monochromator and CCD imager, sequentially. During the measurement of dark-field spectroscopy, the temperature of CCD was cooled down to -70 °C to maximize the signal-to-noise ratio.

Calculation of effective epsilon of metafluid. The theoretically available epsilon enhancement by dispersing AuNP superlattice in water (fig. S33) was retrieved by using s-parameter extraction method, which is based on effective medium theory.[8,9] The required collective set of scattering parameters including transmission, reflections, transmission phase change, and reflection phase change was obtained by FDTD.

UV-Vis absorbance measurement of AuNP clusters and lattices. A Cary-100 UV-Vis (Agilent) spectrophotometer was used for the absorbance measurements of AuNP samples, with a scan rate of 300 nm/min at an interval of 0.5 nm.

S3 Unsuccessful DNA-origami star-motif designs

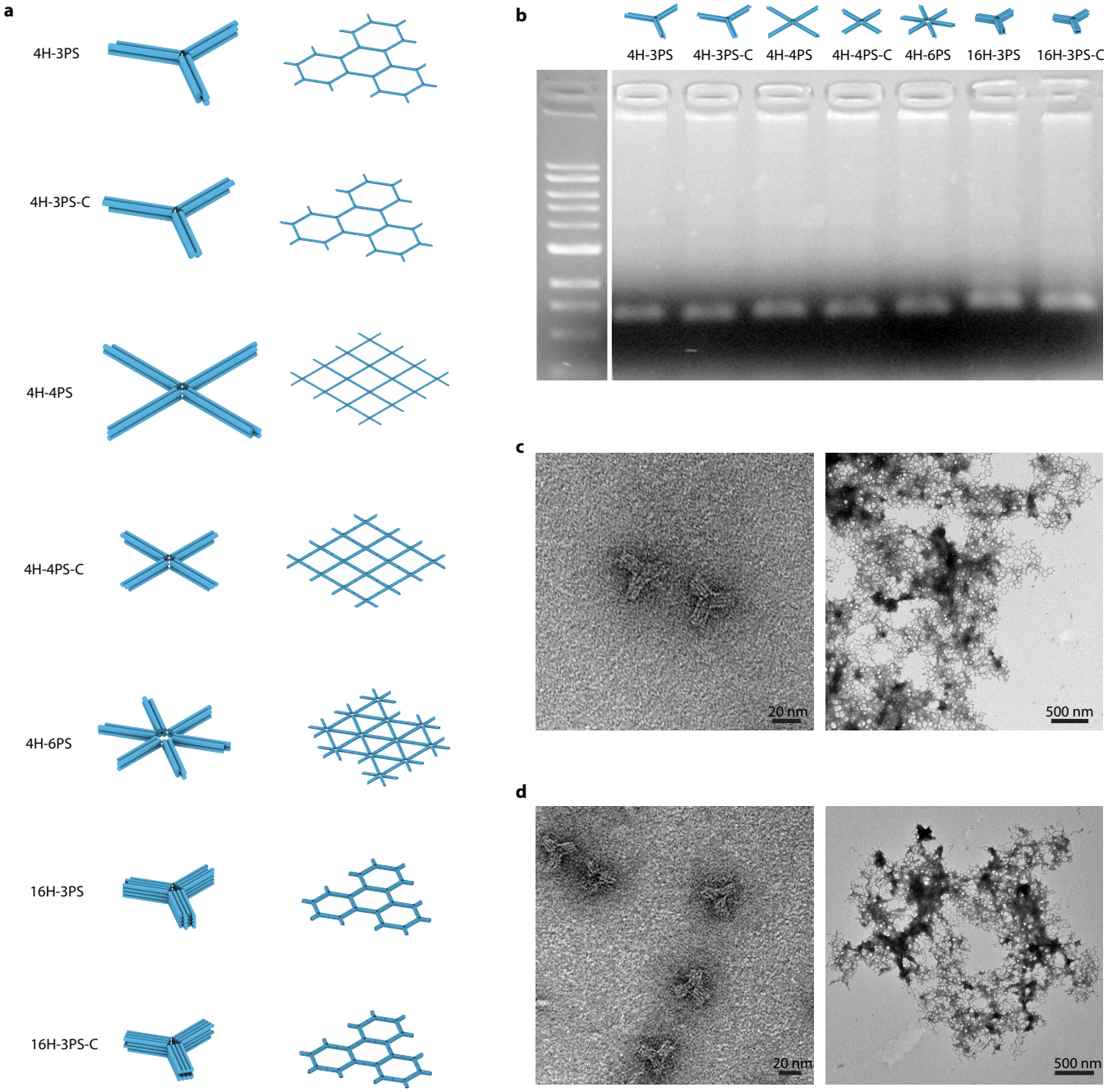

Fig. S2. DNA-origami star-motifs. a, Schematic models of 4H-3PS, 4H-4PS, 4H-6PS, 16H-3PS and its corresponding corrugated designs. **b,** Native agarose gel electrophoresis of 4H-3PS, 4H-4PS, 4H-6PS, 16H-3PS and its corresponding corrugated designs. **c,** 16H-3PS tiles (left) and assembled nanostructures (right). **d,** Corrugated 16H-3PS tiles (left) and assembled nanostructures (right). Connectors utilized in the DNA-origami star-motifs have 3-bp sticky-end with no quasi-gap or gap.

Summary note from unsuccessful tile designs

The initial designs included a 4-helix three-point-star (4H-3PS) tile, 4-helix four-point-star (4H-4PS) tile, and 4-helix six-point-star (4H-6PS) tile (fig. S2a). Though these tiles were formed well on agarose gel electrophoresis (fig. S2b), no large assemblies with well-ordered patterns could be observed (data not shown). A corrugation design strategy was then implemented trying to cancel out curvature accumulation but yielded no improvement (data not shown). We thought this could attribute to the flexibility of the tiles since only 4-helix was used, and thus designed a more rigid 16-helix three-point-star (16H-3PS) tile. Both corrugated and non-corrugated designs of 16H-3PS tile formed small assemblies composing of various polygonal cavities besides the desired hexagon, including square and pentagon, which may prevent the further assembly of 16H-3PS into large and well-ordered hexagonal lattice (fig. S2c and d). The appearance of square and pentagon suggested that either the angle between arms of 16H-3PS were not exactly 120° or the arms had significant in-plane flexibility to favor forming polygons with smaller angles. It is worth noting that for the above tiles, the arms were connected via single-stranded linkage and thus significant in-plane and out-of-plane flexibility could both exist. To address this challenge, the hexagon tile designs studied hereafter were revised to utilize curved continuous helixes to connect arms which would enhance both in-plane and out-of-plane rigidity of the tile.

S4 Strand diagrams of DNA-origami hexagon tiles and connection designs

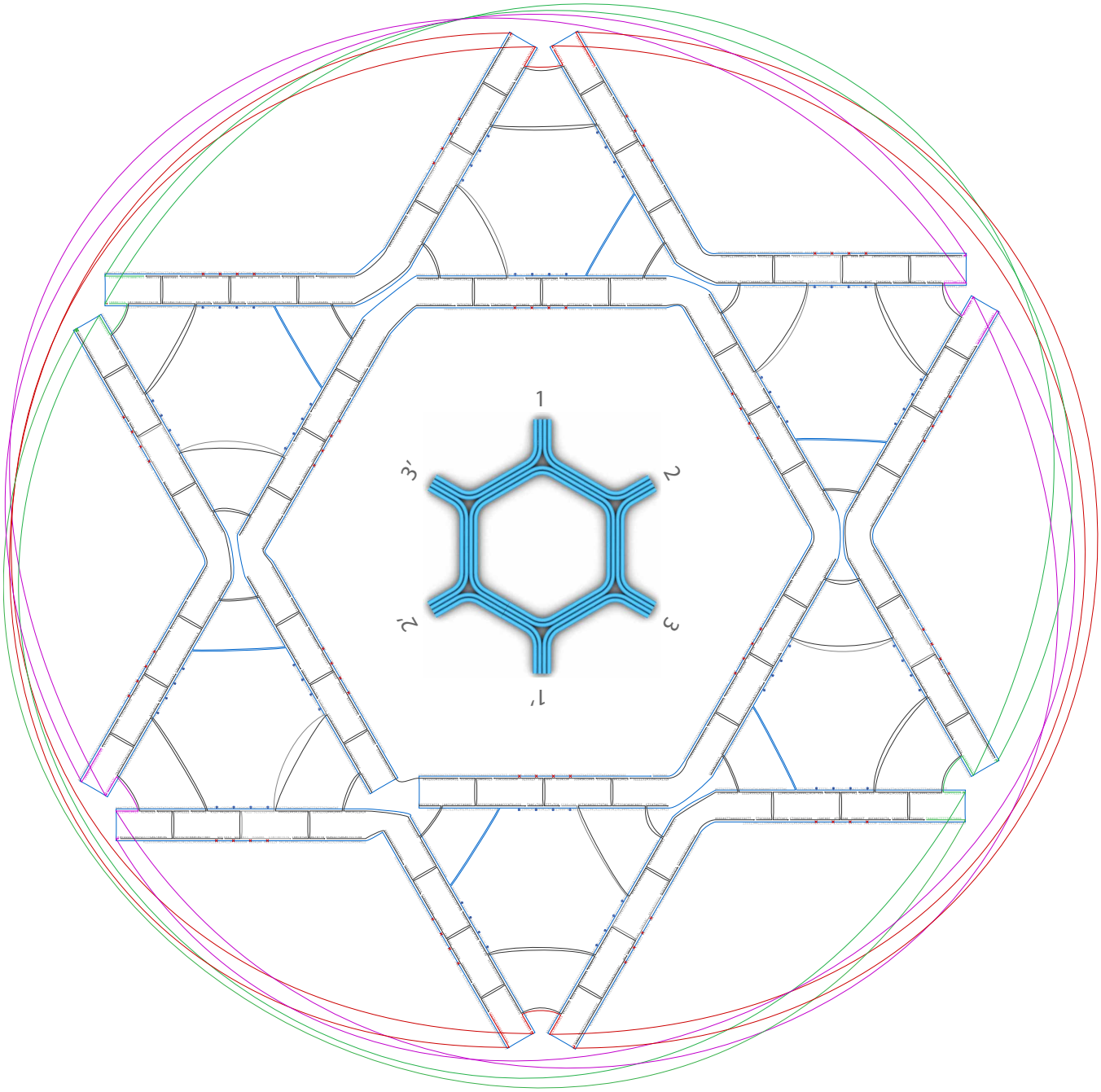

Fig. S3. Strand diagram of the 1×4 HT. Scaffold strand: blue; core staples: black; connector strands: green, red, and pink. An inset diagram is presented to illustrate the connecting strategy between tiles. Arm 1 is connected to arm 1′, Arm 2 is connected to arm 2′, Arm 3 is connected to arm 3′. To prepare monomers, all the core staples were used except the connectors. Zoom in to see details.

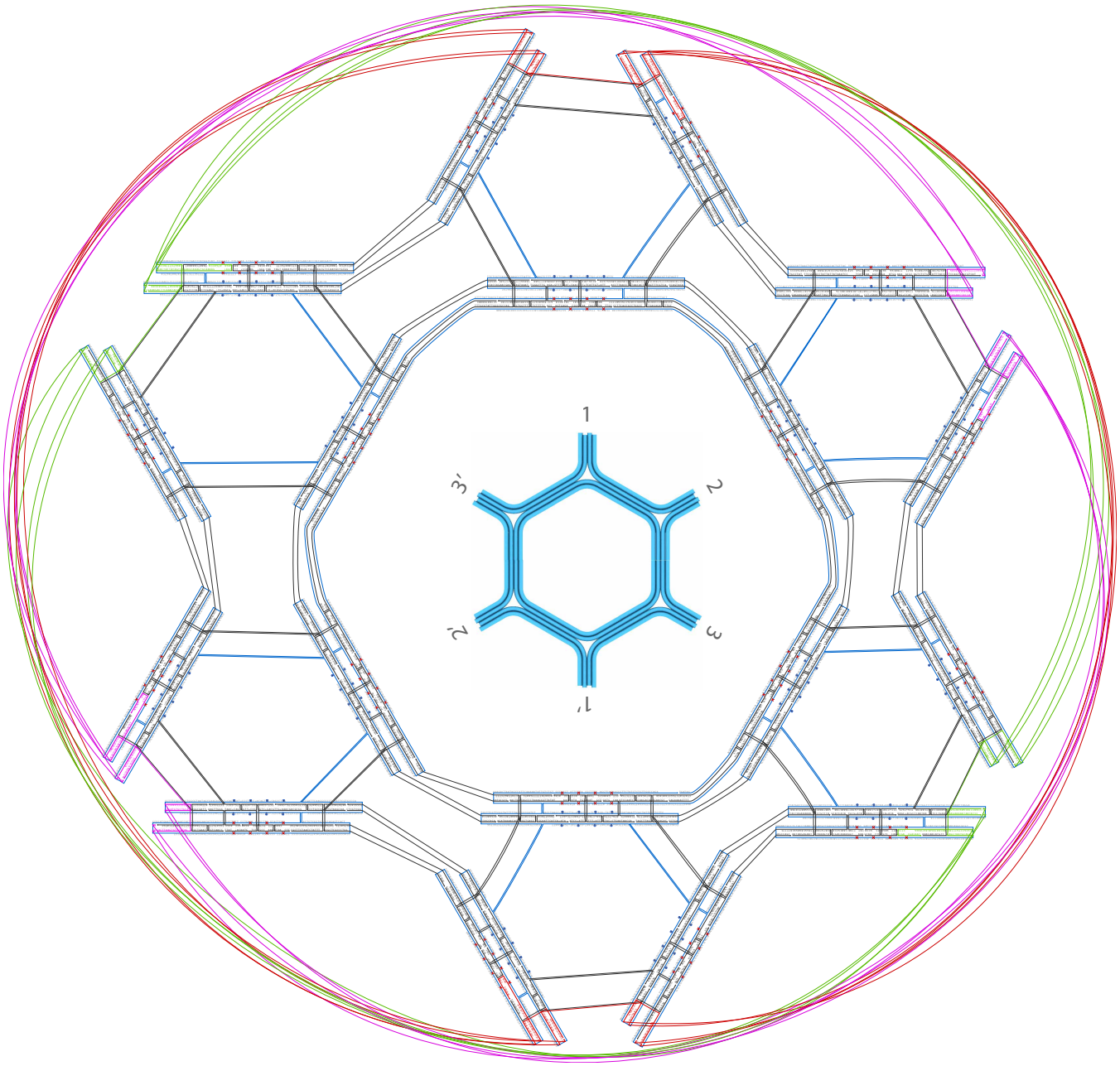

Fig. S4. Strand diagram of the 2×4 HT. Scaffold strand: blue; core staples: black; connector strands: green, red, and pink. An inset diagram is presented to illustrate the connecting strategy between tiles. Arm 1 is connected to arm 1′, Arm 2 is connected to arm 2′, Arm 3 is connected to arm 3′. To prepare monomers, all the core staples were used except the connectors. Zoom in to see details.

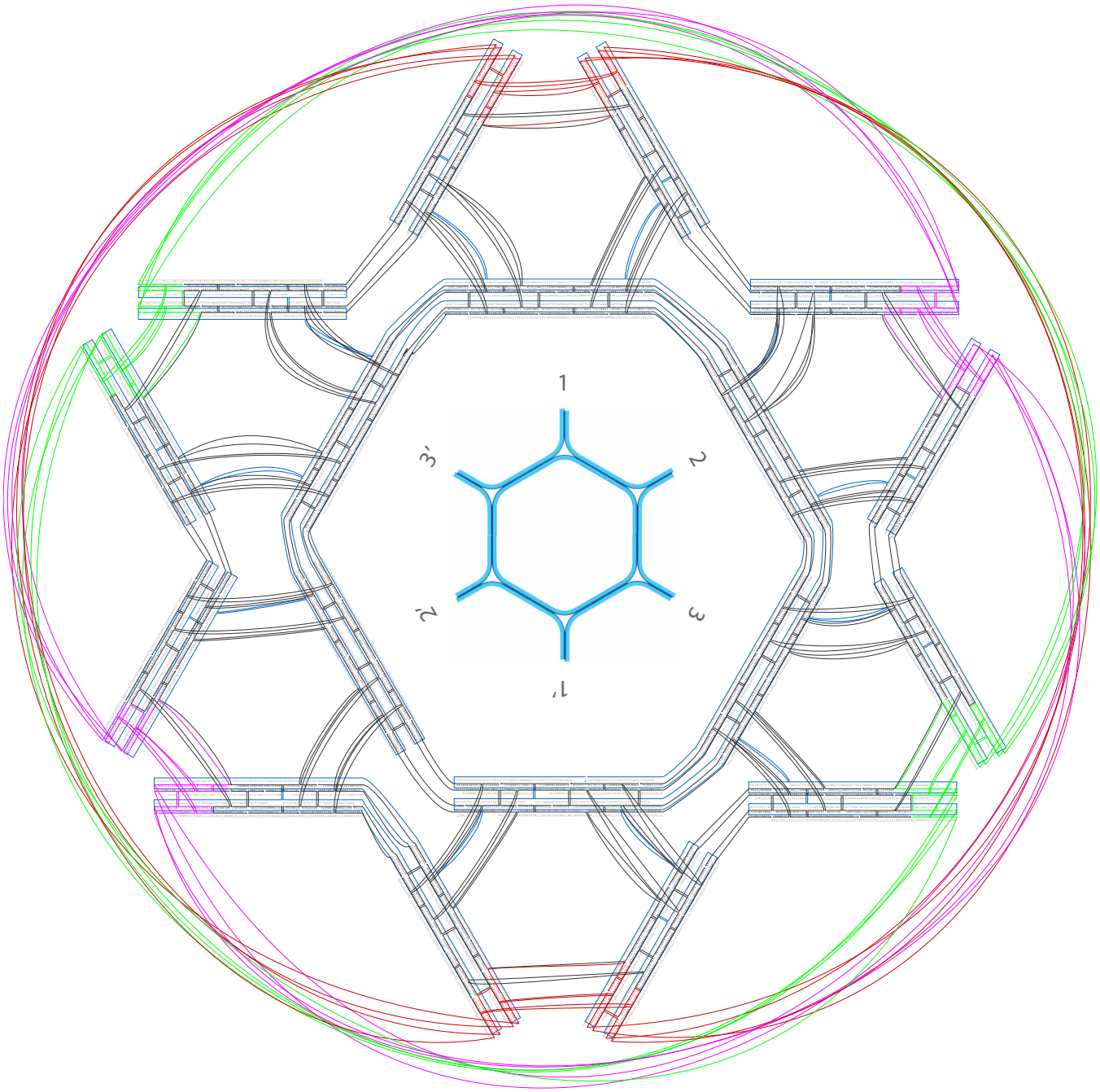

Fig. S5. Strand diagram of the 4×2 HT. Scaffold strand: blue; core staples: black; connector strands: green, red, and pink. An inset diagram is presented to illustrate the connecting strategy between tiles. Arm 1 is connected to arm $1'$, Arm 2 is connected to arm $2'$, Arm 3 is connected to arm $3'$. To prepare monomers, all the core staples were used except the connectors. Zoom in to see details.

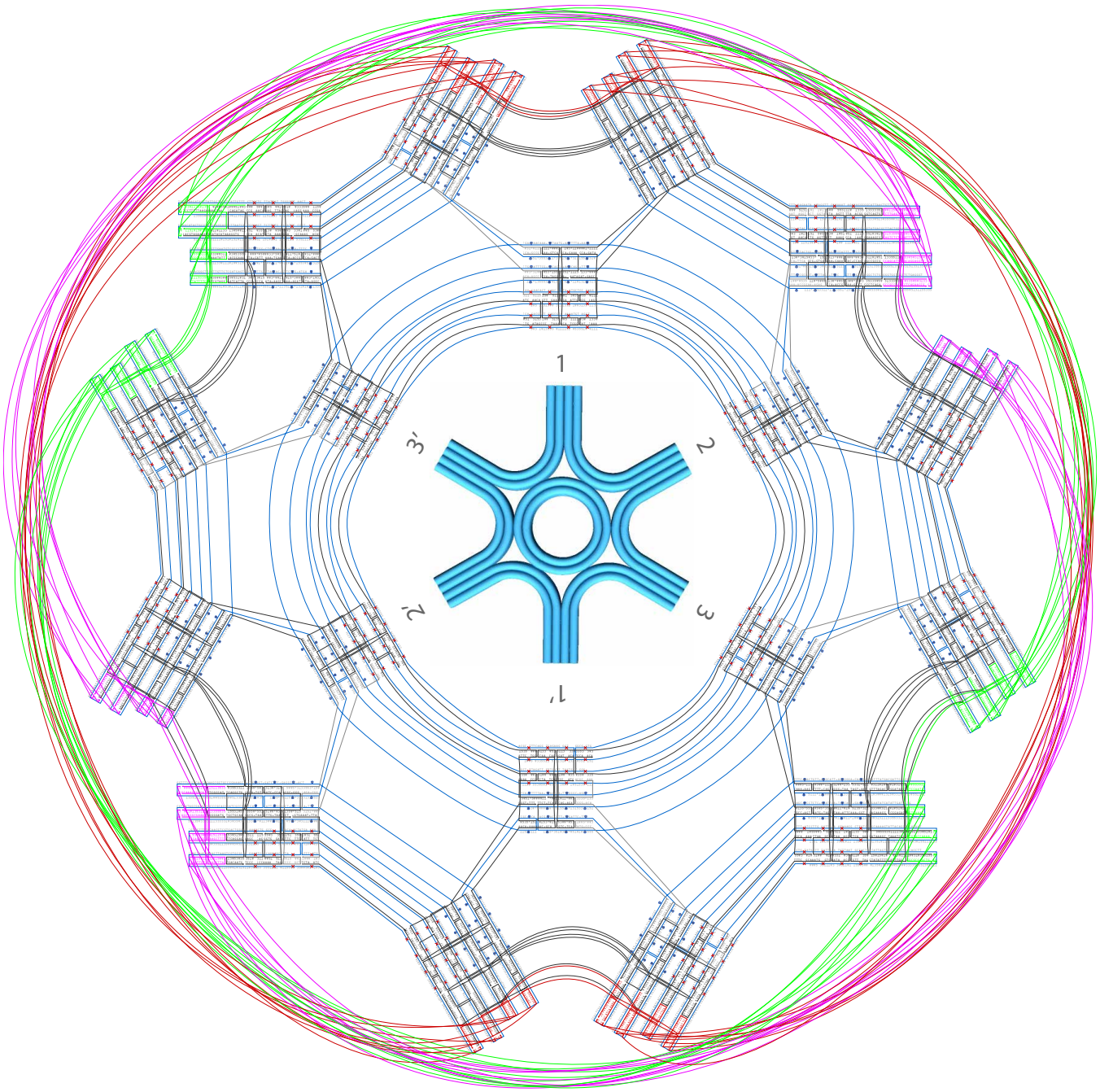

Fig. S6. Strand diagram of the failed 4×4 HT. Scaffold strand: blue; core staples: black; connector strands: green, red, and pink. An inset diagram is presented to illustrate the connecting strategy between tiles. Arm 1 is connected to arm 1′, Arm 2 is connected to arm 2′, Arm 3 is connected to arm 3′. To prepare monomers, all the core staples were used except the connectors. Zoom in to see details.

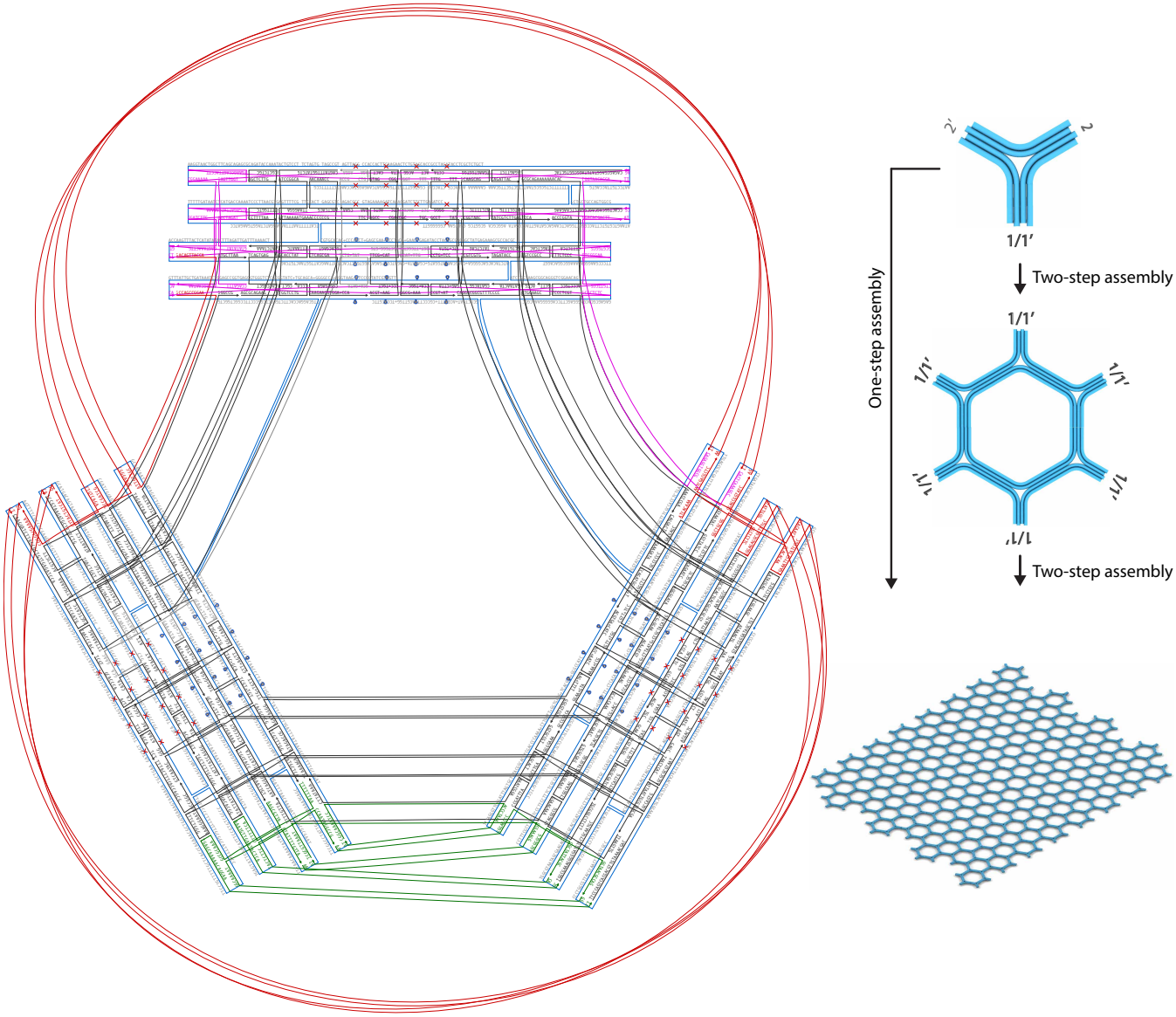

Fig. S7. Strand diagram of the 4×4H-3PS DNA-origami tile and its assembly pathways towards 2D lattice. Scaffold strand: blue; core staples: black; connector strands: green, red, and pink. Diagrams on the right are presented to illustrate two assembly pathways to form 2D lattices. In the one-step assembly, three-arm motifs assembled to 2D lattices by adding all connecting staple strands. In the first step of the two-step assembly, 4×4H-3PS tiles assembled to hexagon tiles by adding red and pink connector staple strands to connect arm 2 and arm 2′. Hexagon tiles were then purified and mixed with green connector staple strands to connect arm 1 and 1′ to form 2D lattices. Zoom in to see details.

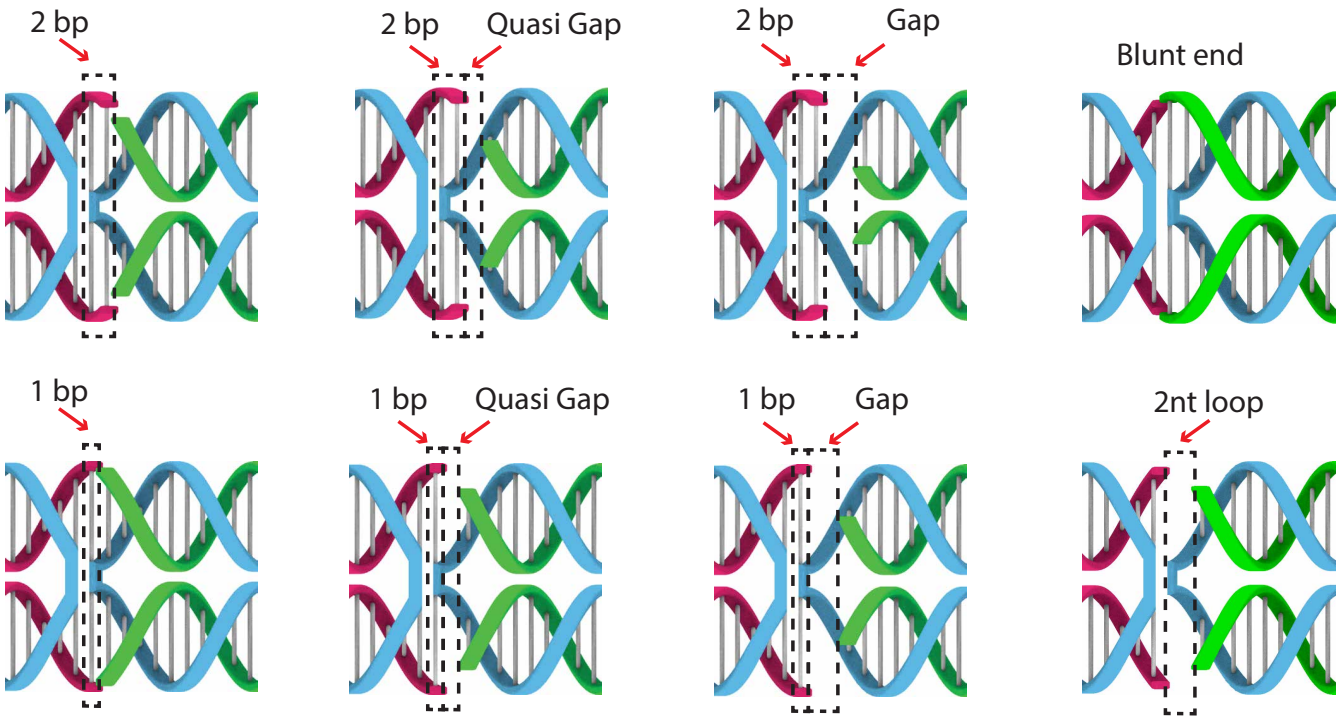

Fig. S8. Connector strand designs. Scaffold strand: blue; staples: red and green. A total of eight connection designs were utilized in this study with sticky-end strength ranging from 2-base-pair (2-bp), 1-bp, to 0-bp (blunt end). The connection flexibility are induced via leaving one (quasi gap) or two (gap) unpaired scaffold base. For the 2-nt loop connector design, a 2-nucleotide (2-nt) unpaired scaffold loop was induced to prevent stacking between arms.

S5 Structure modeling of DNA-origami hexagon tiles and lattices

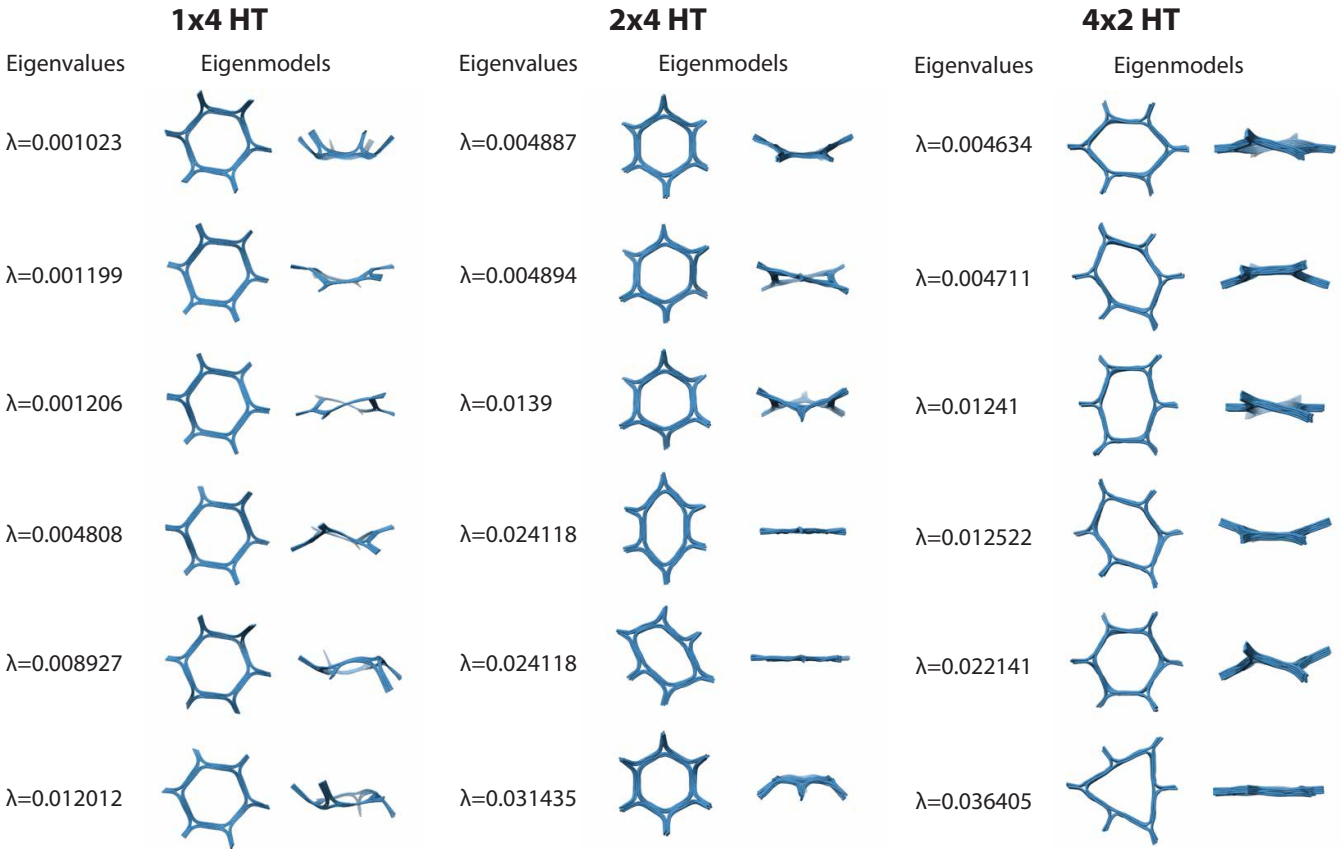

Fig. S9. Normal modes and eigenvalues for the 1×4 HT, 2×4 HT, and 4×2 HT.

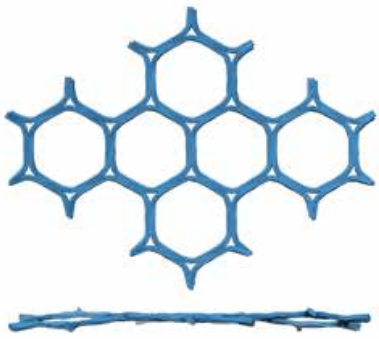

2 tile x 2 tile lattice of 2x4 HT

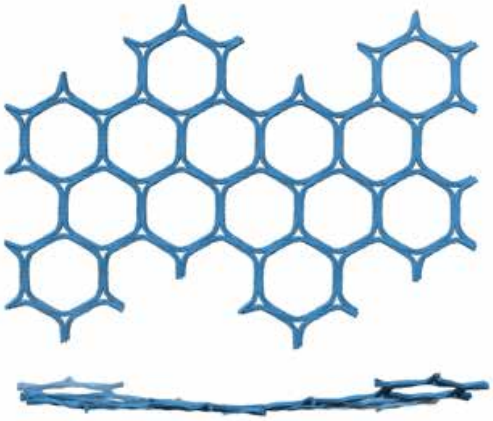

4 tile x 2 tile lattice of 2x4 HT

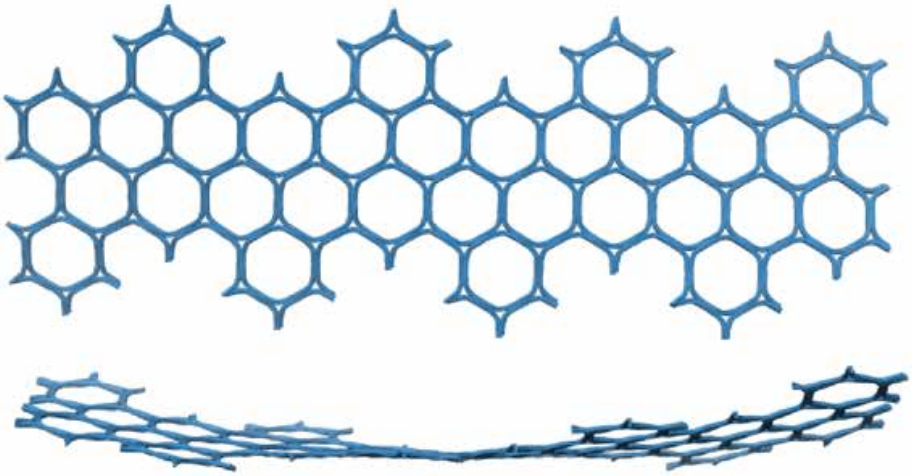

8 tile x 2 tile lattice of 2x4 HT

Fig. S10. Solution shapes for the 2×4 HT lattices with increasing aspect ratio.

S6 TEM images of tubes and 2D lattices assembled from DNA-origami hexagon tiles

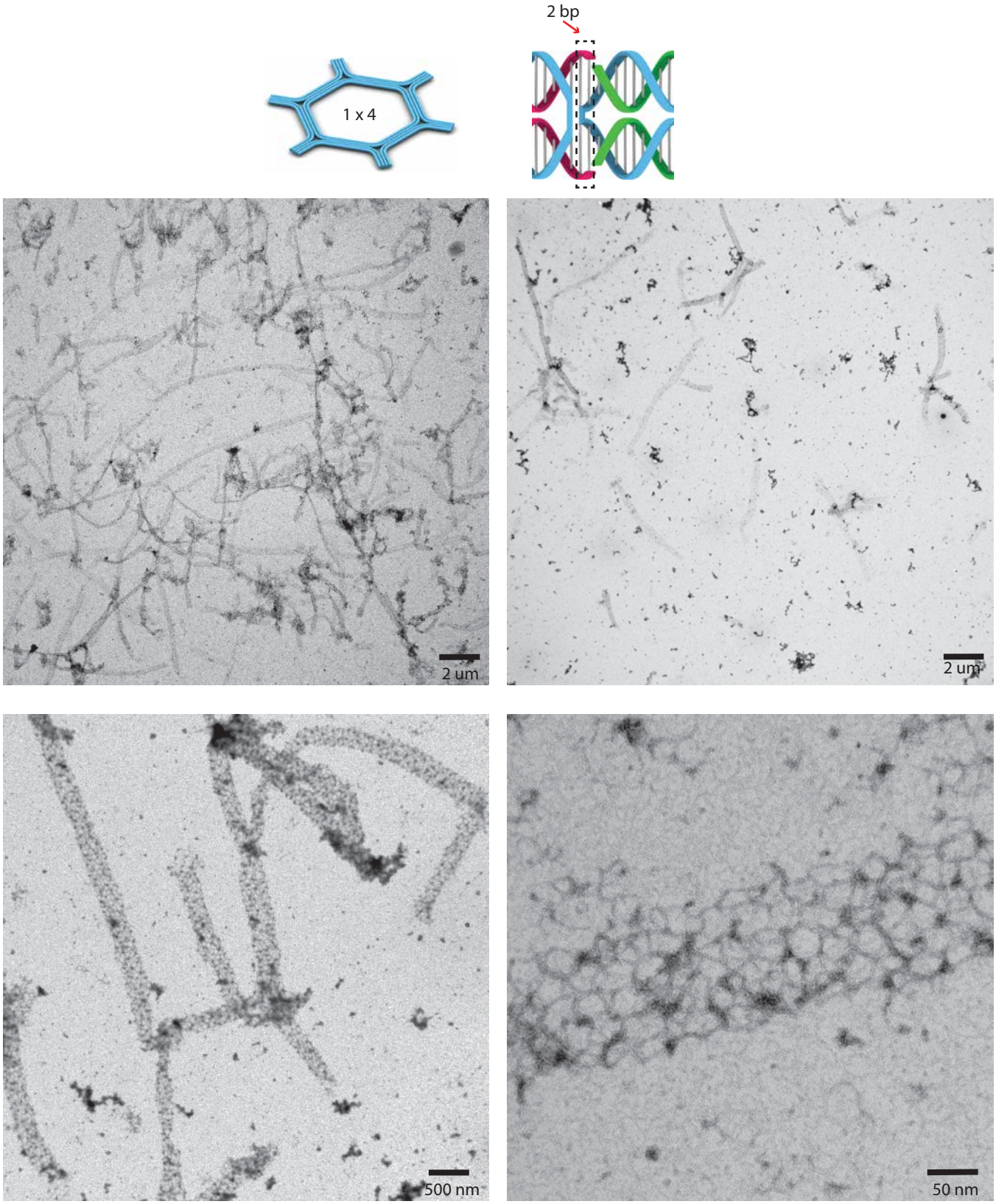

Fig. S11. TEM images of tubes assembled from the 1×4 HT using 2-bp connectors.

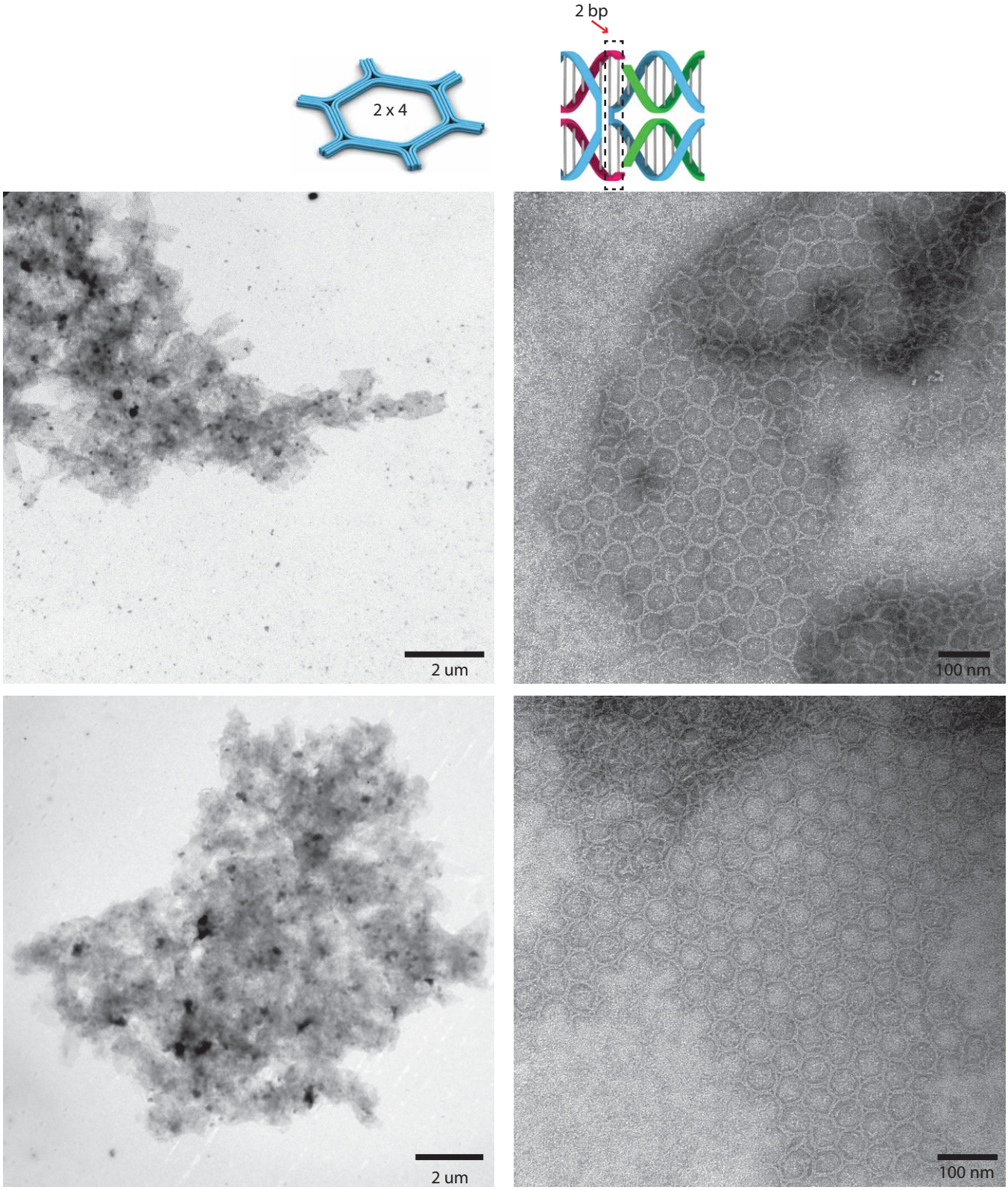

Fig. S12. TEM images of aggregates/small lattices assembled from the 2×4 HT using 2-bp connectors.

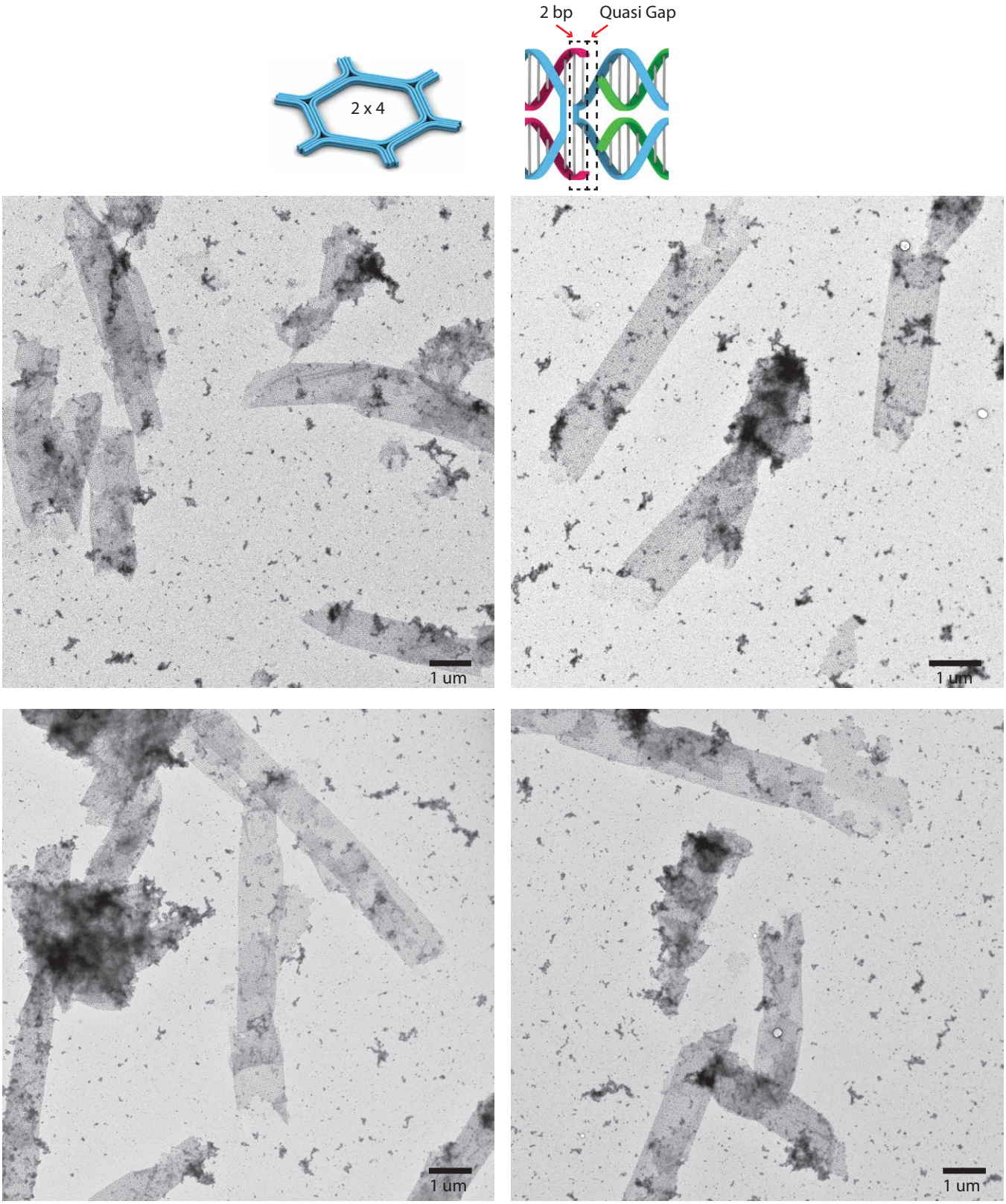

Fig. S13. TEM images of tubes assembled from the 2×4 HT using 2-bp-quasi-gap connectors.

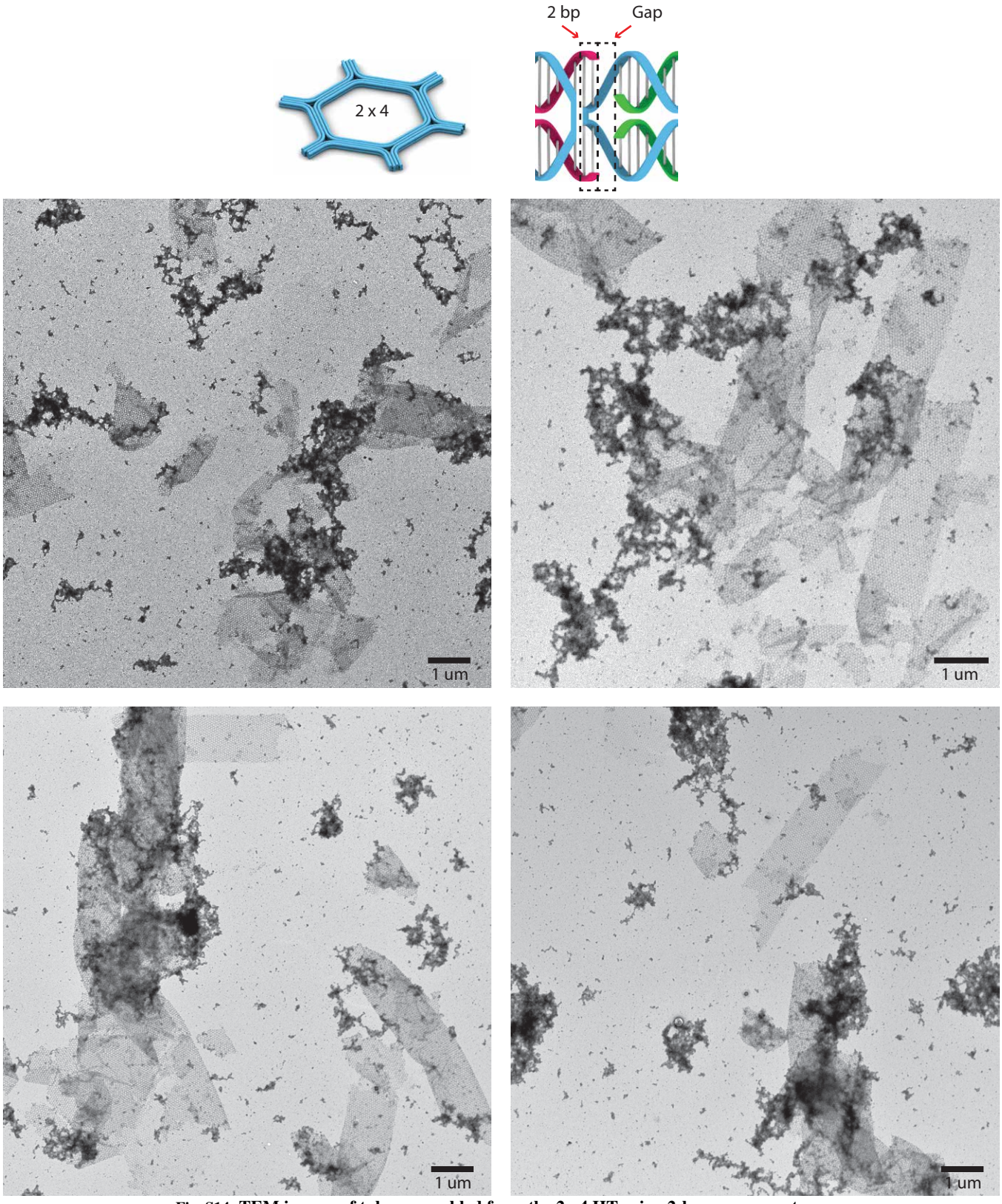

Fig. S14. TEM images of tubes assembled from the 2×4 HT using 2-bp-gap connectors.

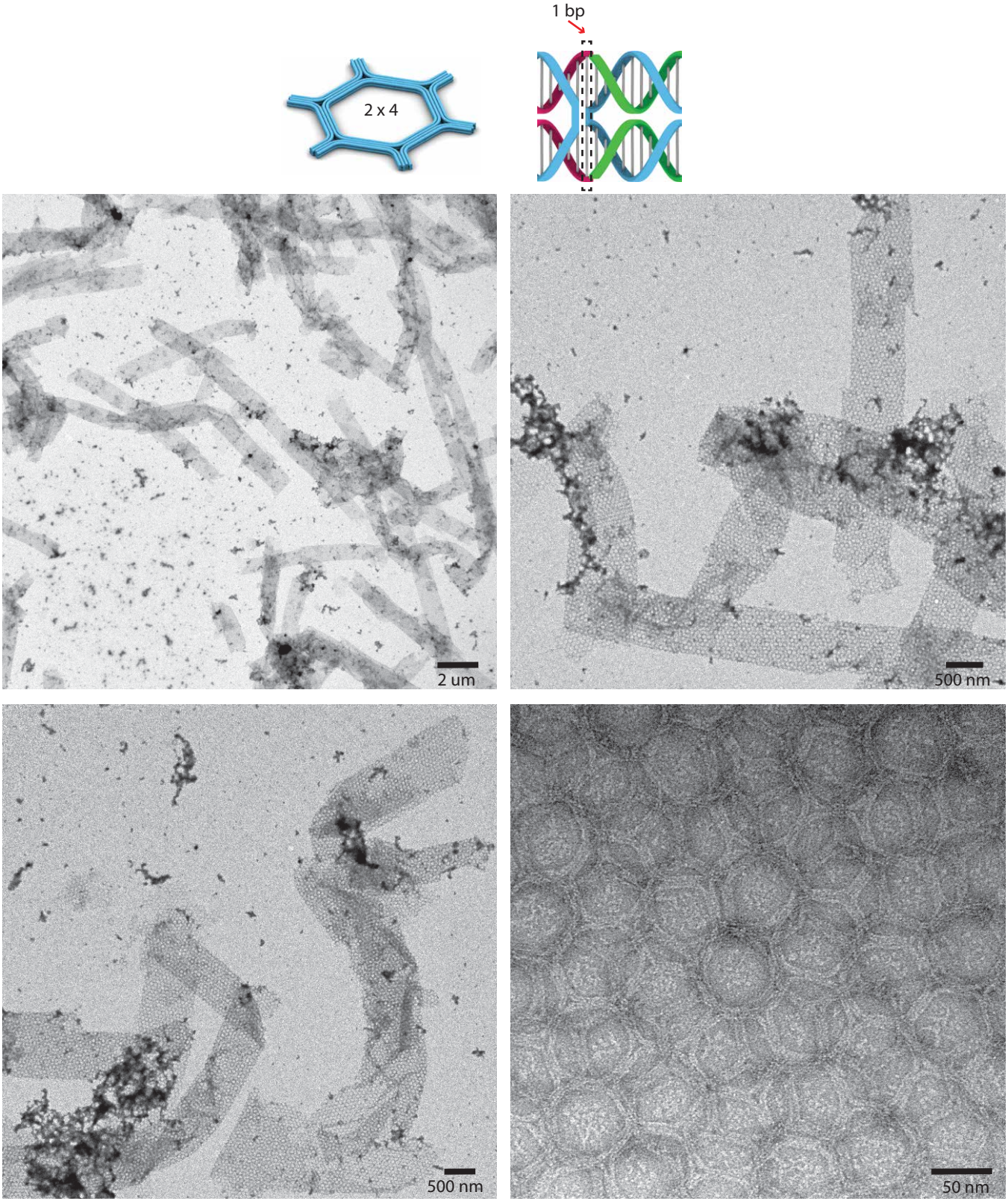

Fig. S15. TEM images of tubes assembled from the 2×4 HT using 1-bp connectors.

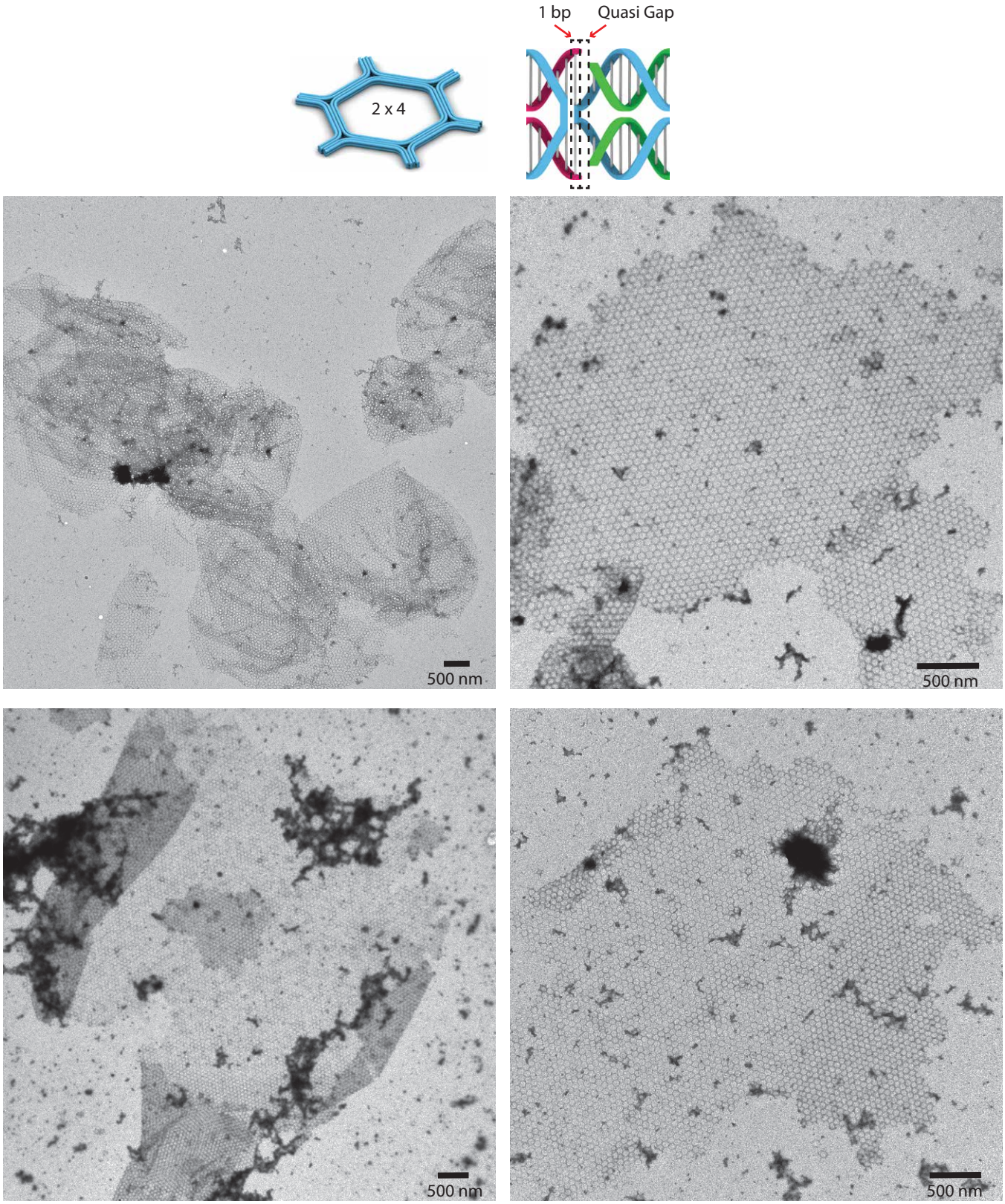

Fig. S16. TEM images of 2D lattices assembled from the 2×4 HT using 1-bp-quasi-gap connectors.

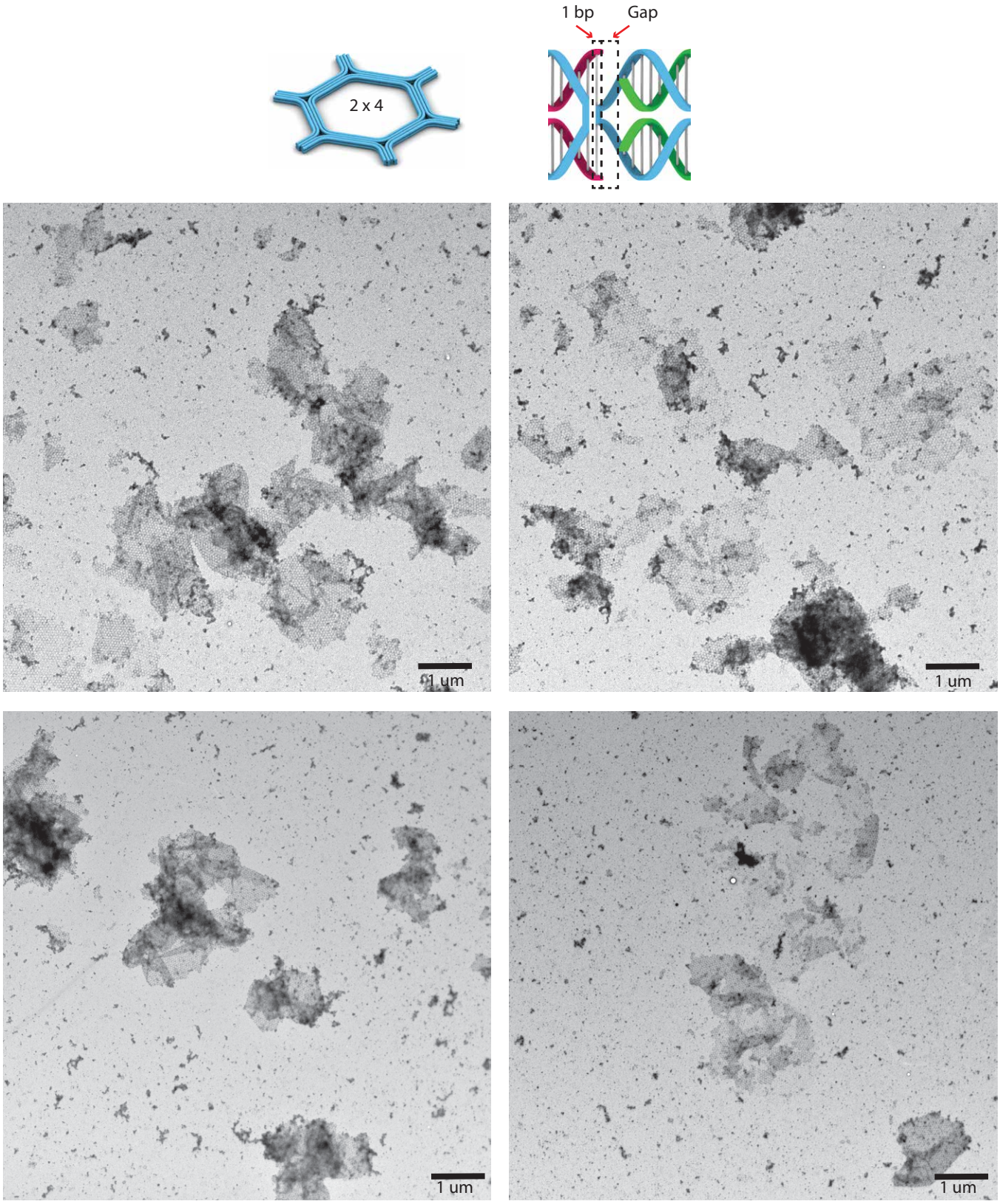

Fig. S17. TEM images of 2D lattices assembled from the 2×4 HT using 1-bp-gap connectors.

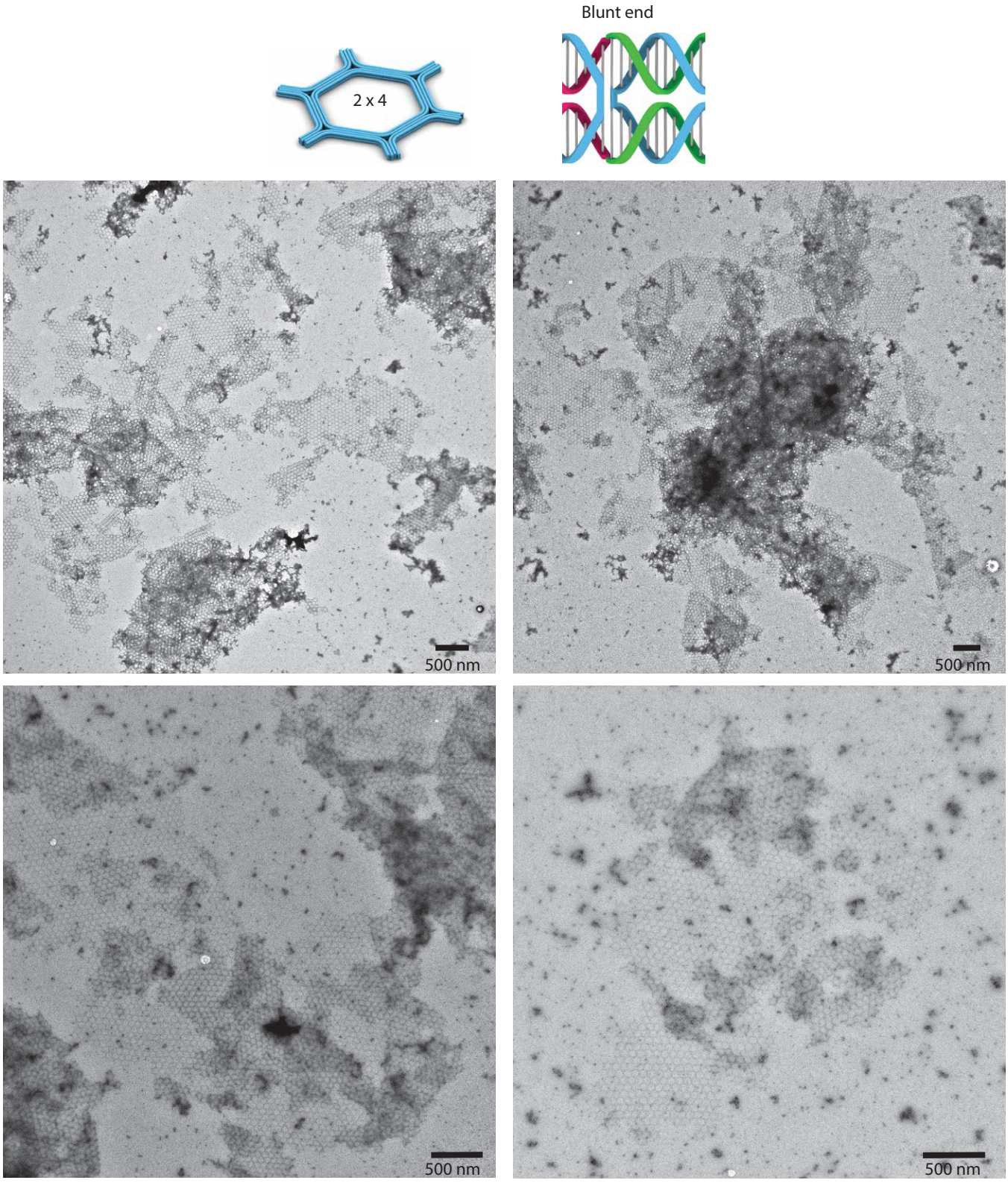

Fig. S18. TEM images of 2D lattices assembled from the 2×4 HT using blunt end connectors.

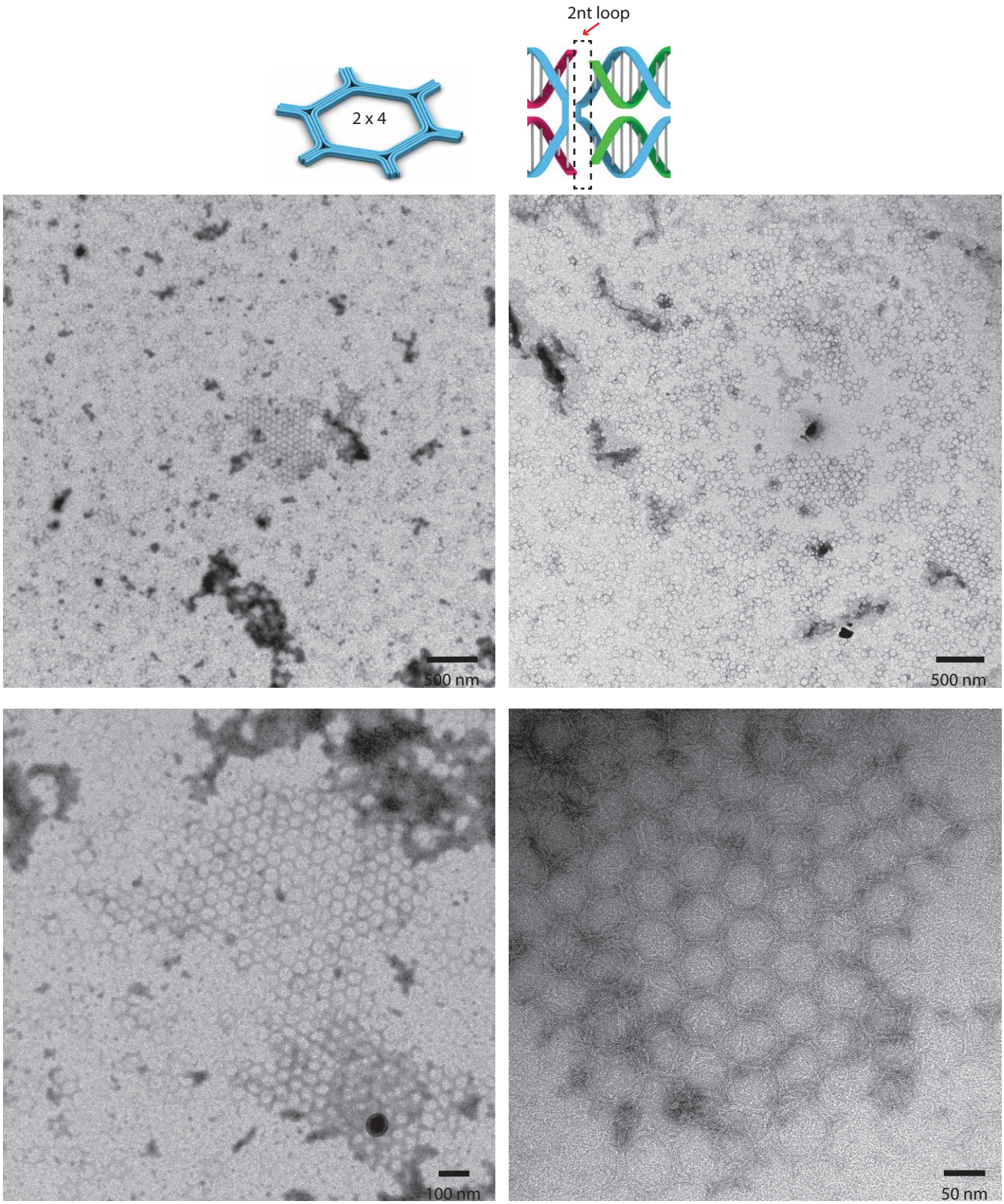

Fig. S19. TEM images of 2D lattices assembled from the 2×4 HT using 2-nt loop connectors.

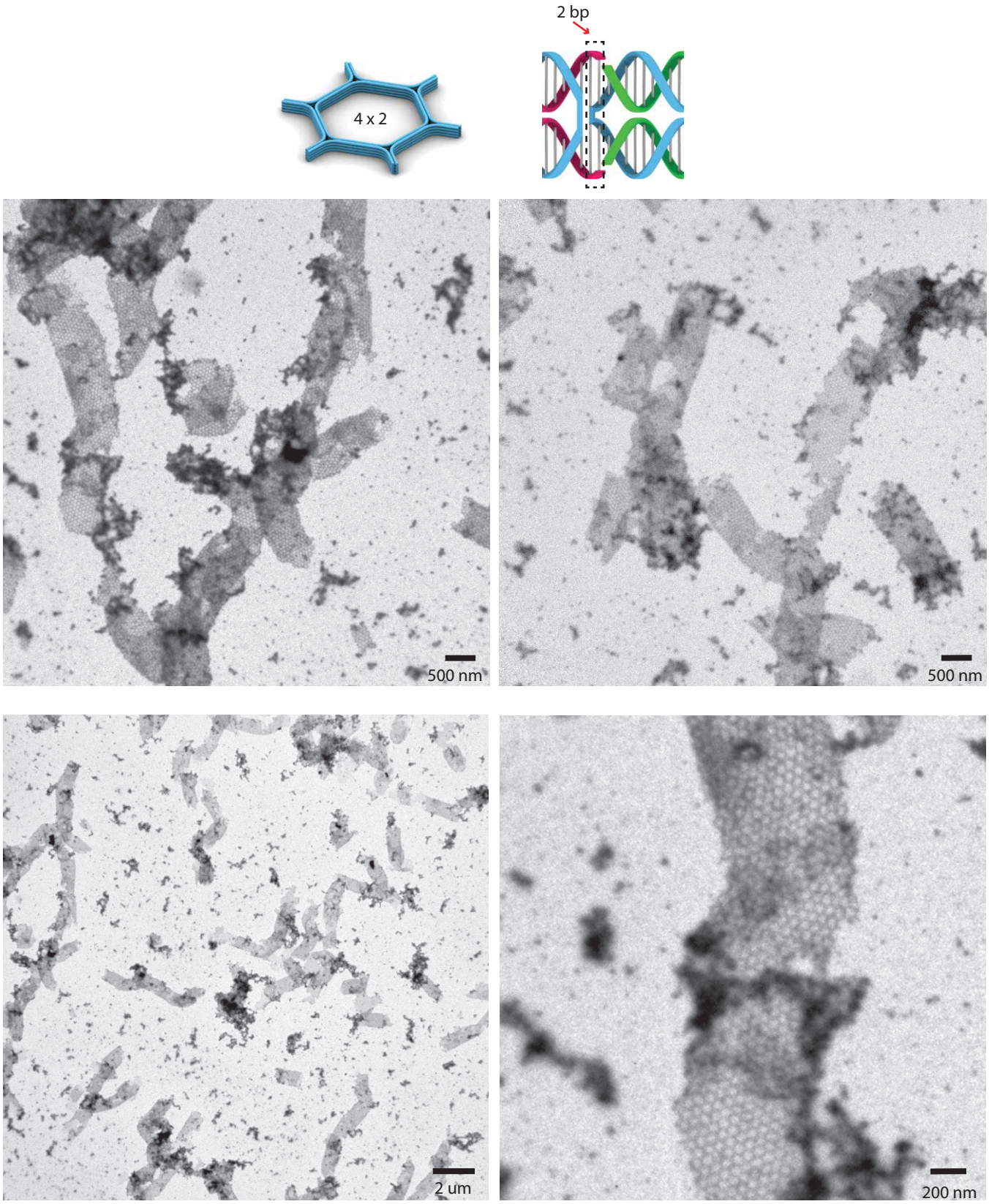

Fig. S20. TEM images of tubes assembled from the 4×2 HT using 2-bp connectors.

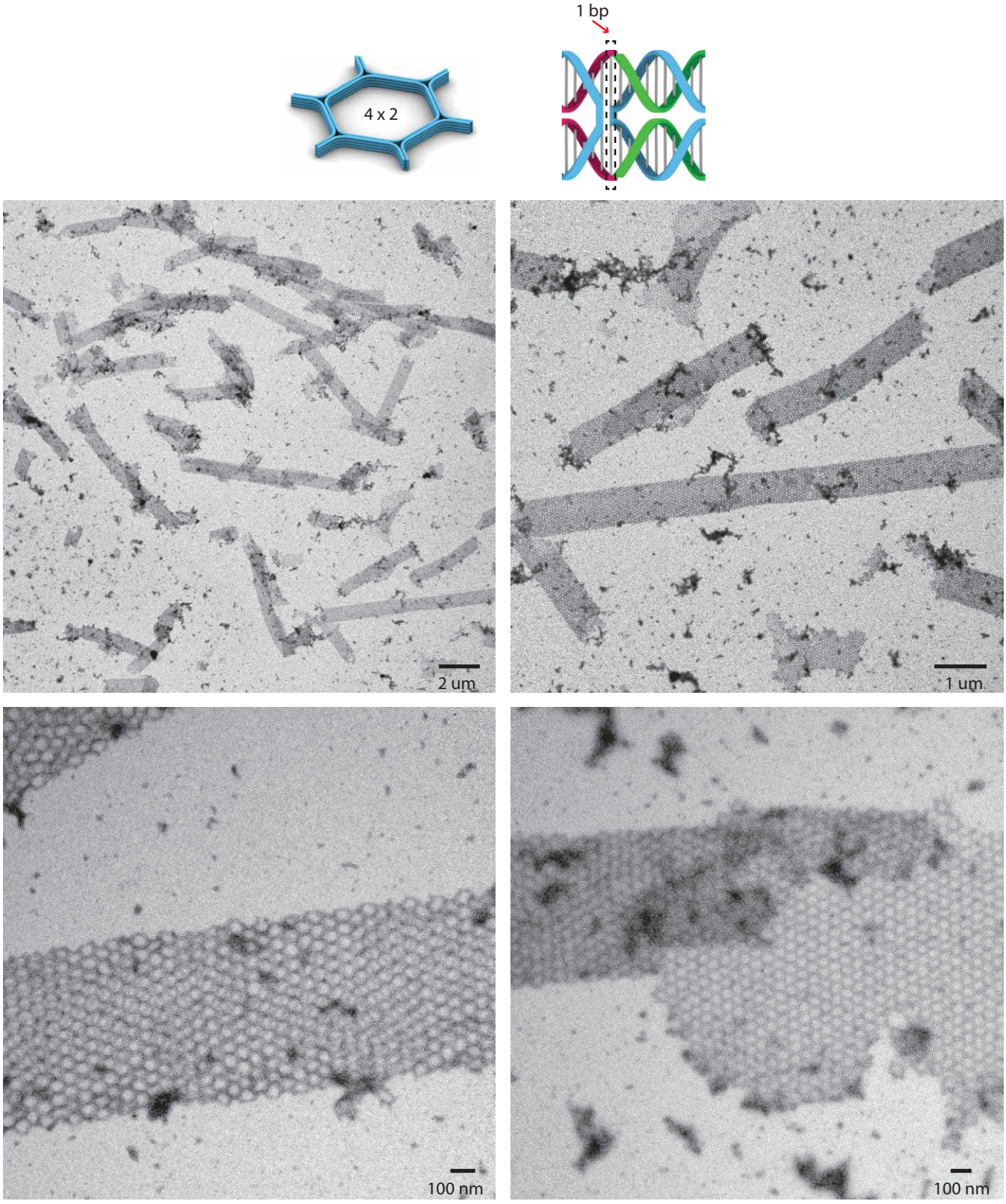

Fig. S21. TEM images of tubes assembled from the 4×2 HT using 1-bp connectors.

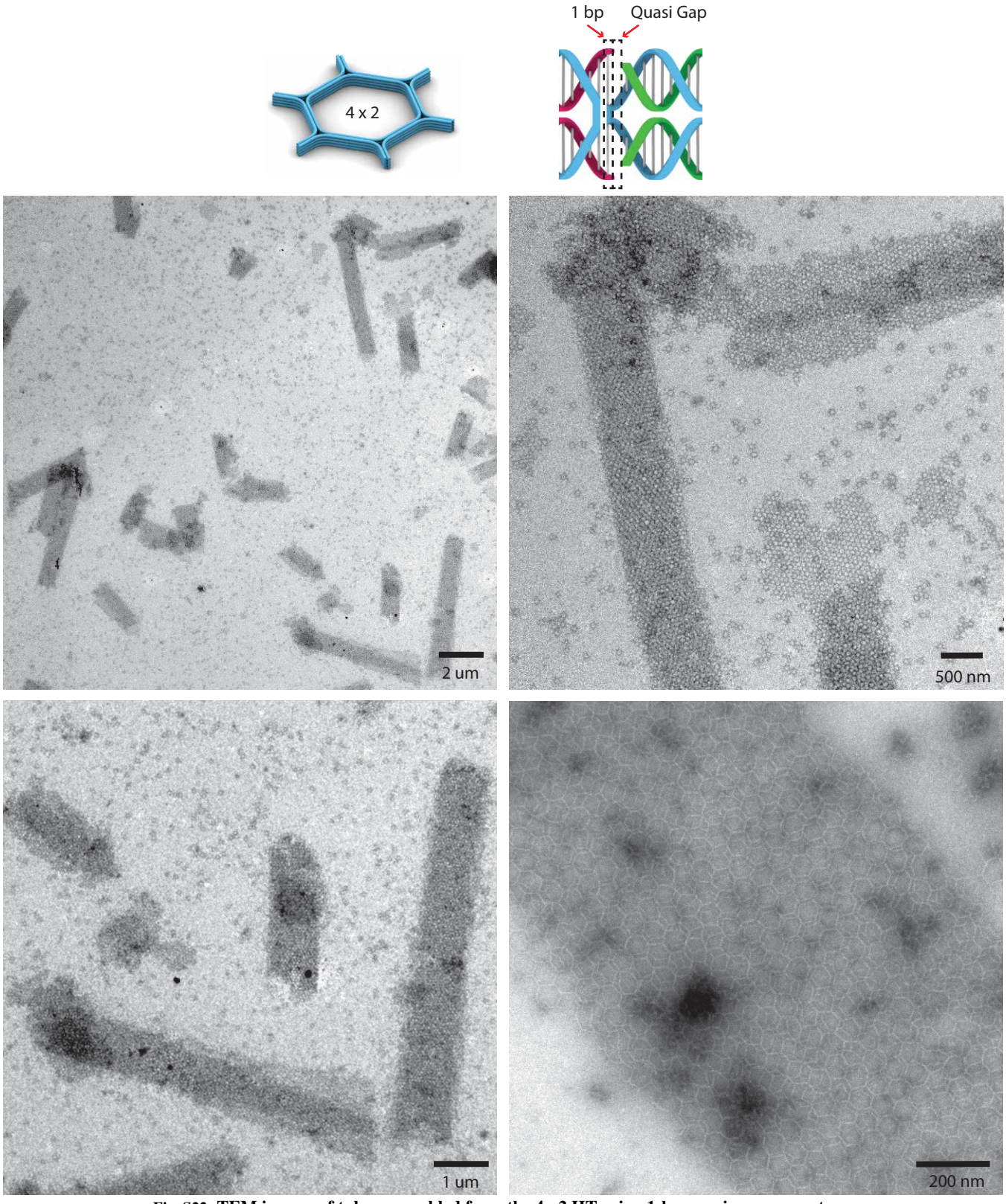

Fig. S22. TEM images of tubes assembled from the 4×2 HT using 1-bp-quasi-gap connectors.

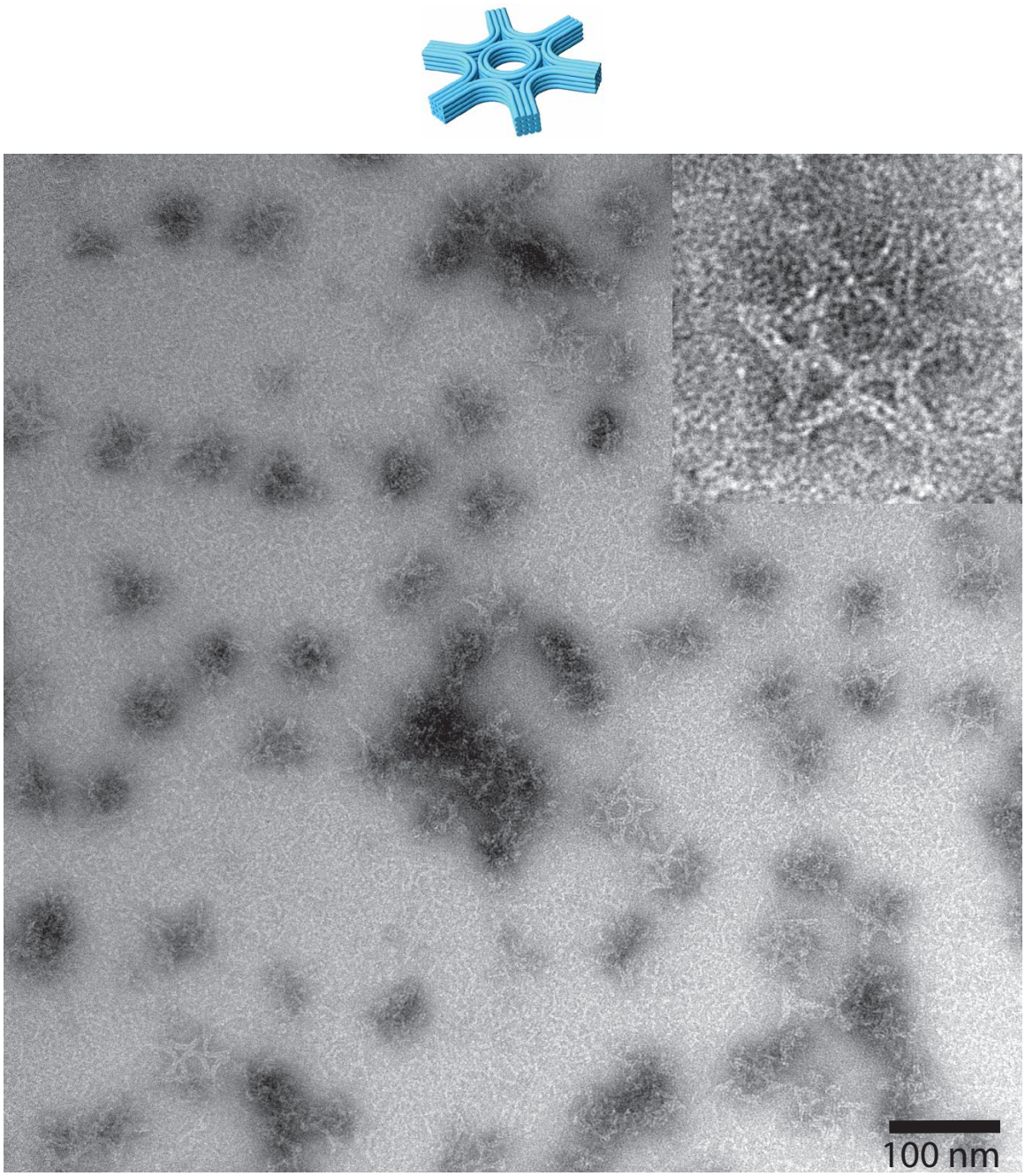

Fig. S23. TEM image of the failed 4×4 HT tile. Due to large degree of in-plane curvature induced for the hexagon tile design, most of the tiles were illy-formed and had difficulty to maintain intact hexagon shape.

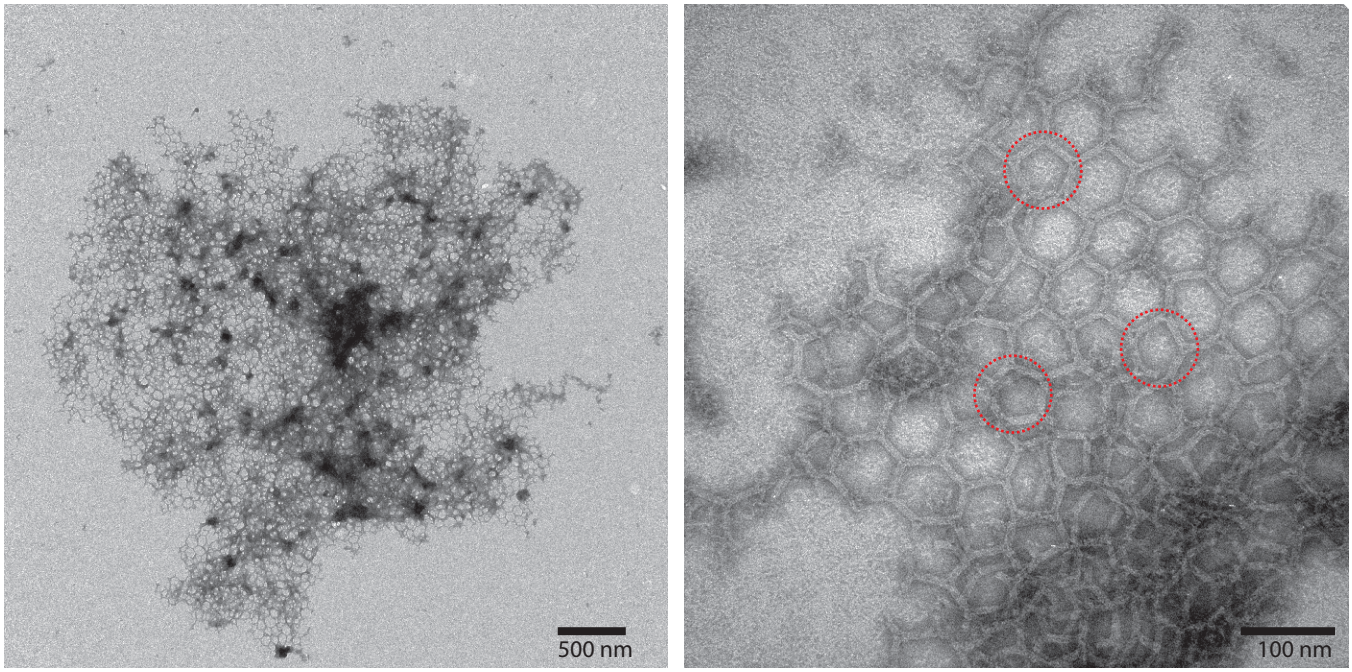

Fig. S24. TEM images of 2D lattices assembled from the 4×4H-3PS DNA-origami tile in a one-step reaction as depicted in fig. S7. Pentamers were highlighted in red circles.

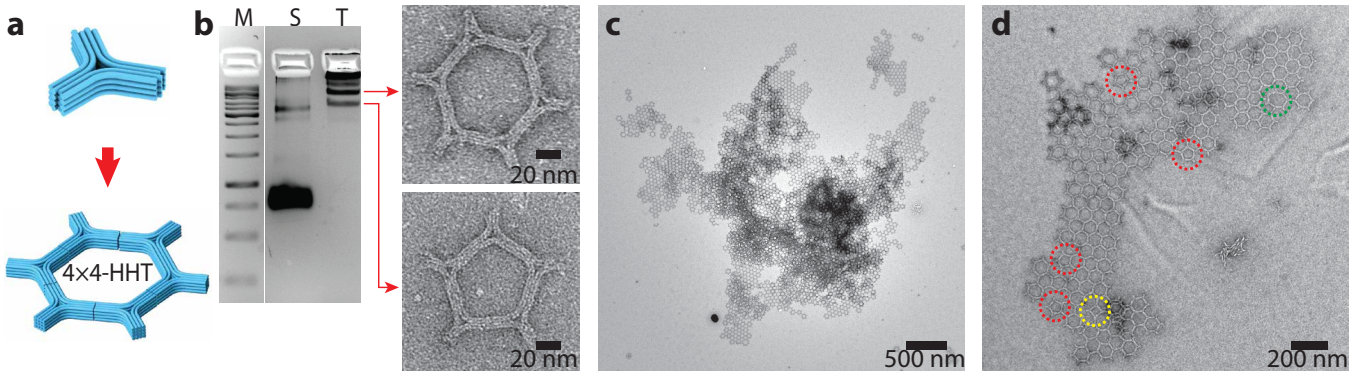

Fig. S25. Assembly of 4×4 HT in a two-step reaction as depicted in fig. S7. a, A model illustrates the assembly of 4×4 HT from the 4×4H-3PS DNA-origami tile. **b,** Agarose gel electrophoresis shows the corresponding bands of hexamer and pentamer assembled from the 4×4H-3PS DNA-origami tile, with red arrows point to the corresponding TEM images. Lane M contains 1kb DNA ladder. Lane S contains p7560 scaffold. Lane T contains structures assembled from the 4×4H-3PS DNA-origami tile. **c** and **d,** TEM images of 2D lattices assembled from purified hexamers of the 4×4H-3PS tiles. Pentamers were highlighted by red circles. A tetramer (marked by a yellow circle) and a heptamer (marked by a green circle) was also found in the lattice.

S7 AuNP clusters and superlattices

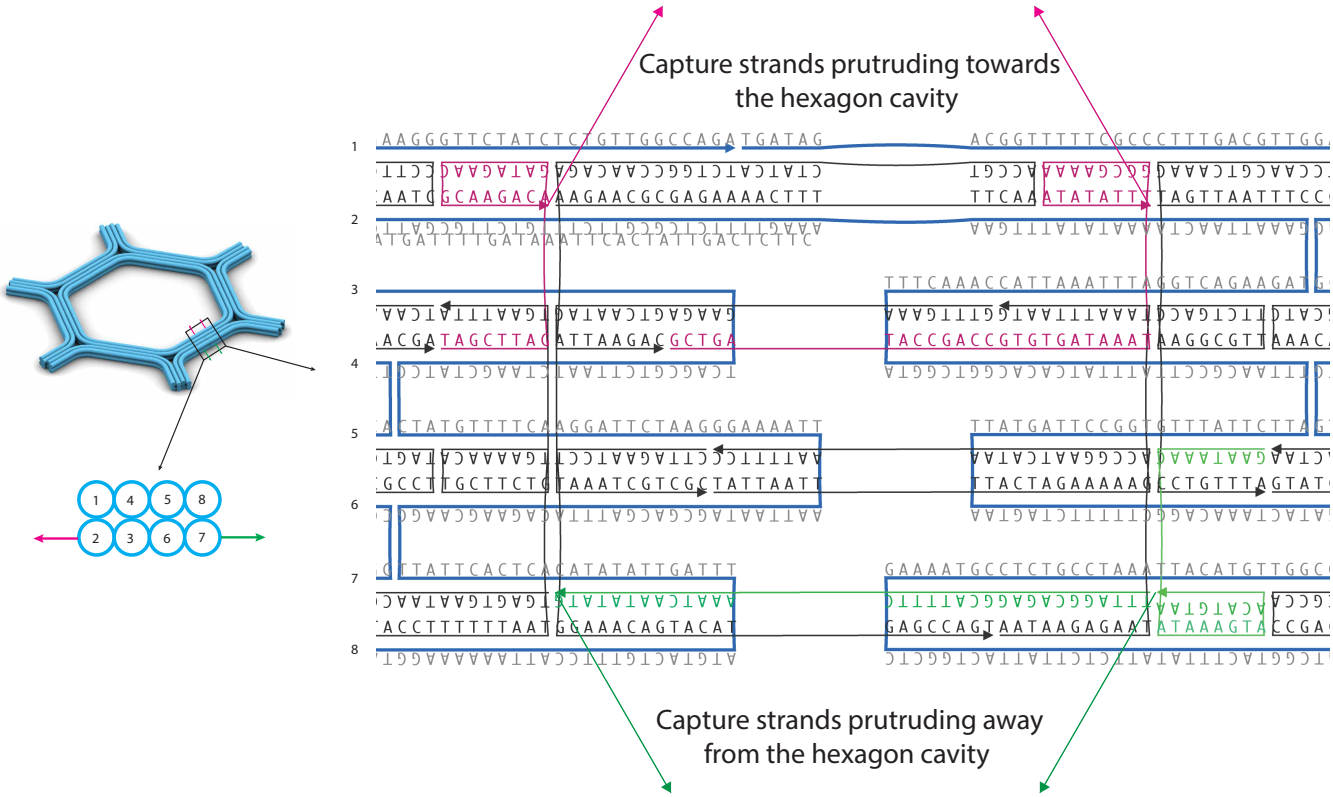

Fig. S26. Schematic illustration of AuNP capture strands on the 2×4 HT. Capture strands were 20- or 40-base-long single-stranded extensions from the 3' end of selected staple strands (i.e. pink and green strands). Extensions were generated from staples located on the bottom layer of helixes to protrude towards (pink strands on Helix-2) or away (green strands on Helix-7) from the hexagon within the same plane. The two pink (or green) capture strands were 32-bases away from each other.

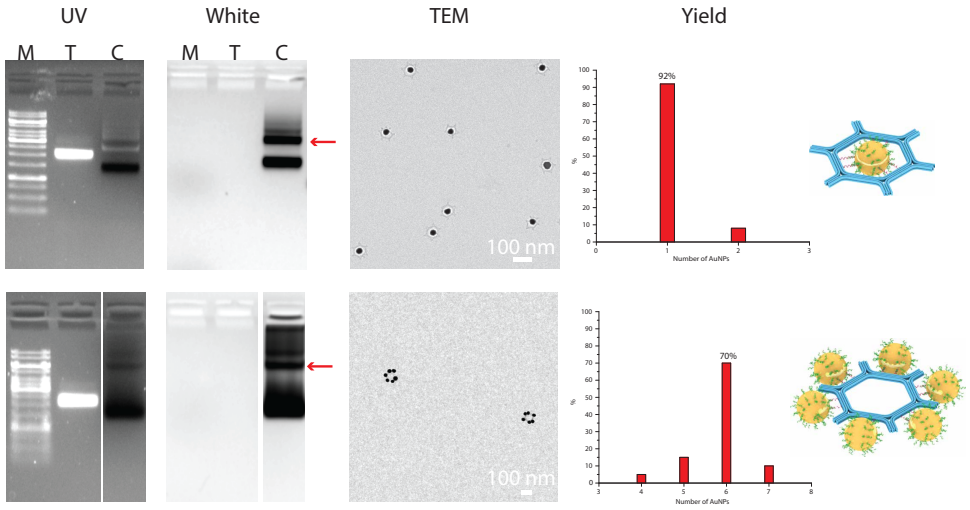

Fig. S27. Agarose gel and TEM images of AuNP clusters assembled on the 2×4 HT monomers. For each AuNP cluster design, the agarose gel was imaged under both UV and white light excitation. Lane M contains 1 kb DNA marker; Lane T contains hexagon tile; Lane C contains AuNP cluster. The corresponding band for AuNP cluster was extracted from the gel and imaged by TEM. Yield of correct AuNP clusters was quantified based on TEM images.

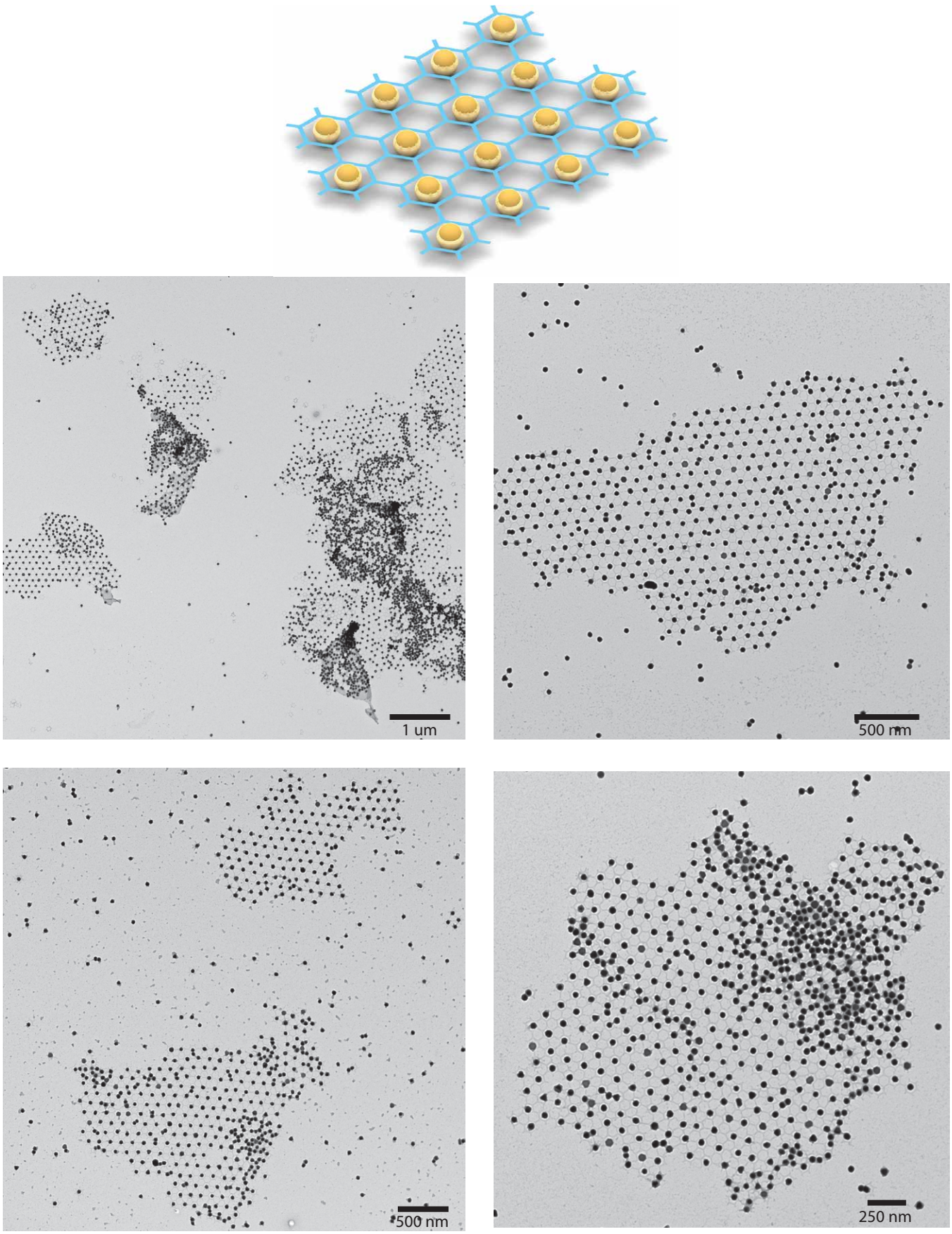

Fig. S28. TEM images of 30nm_Au_2D_1 AuNP superlattice assembled on the 2×4 HT hexagonal origami 2D lattices. A schematic model is presented on the top.

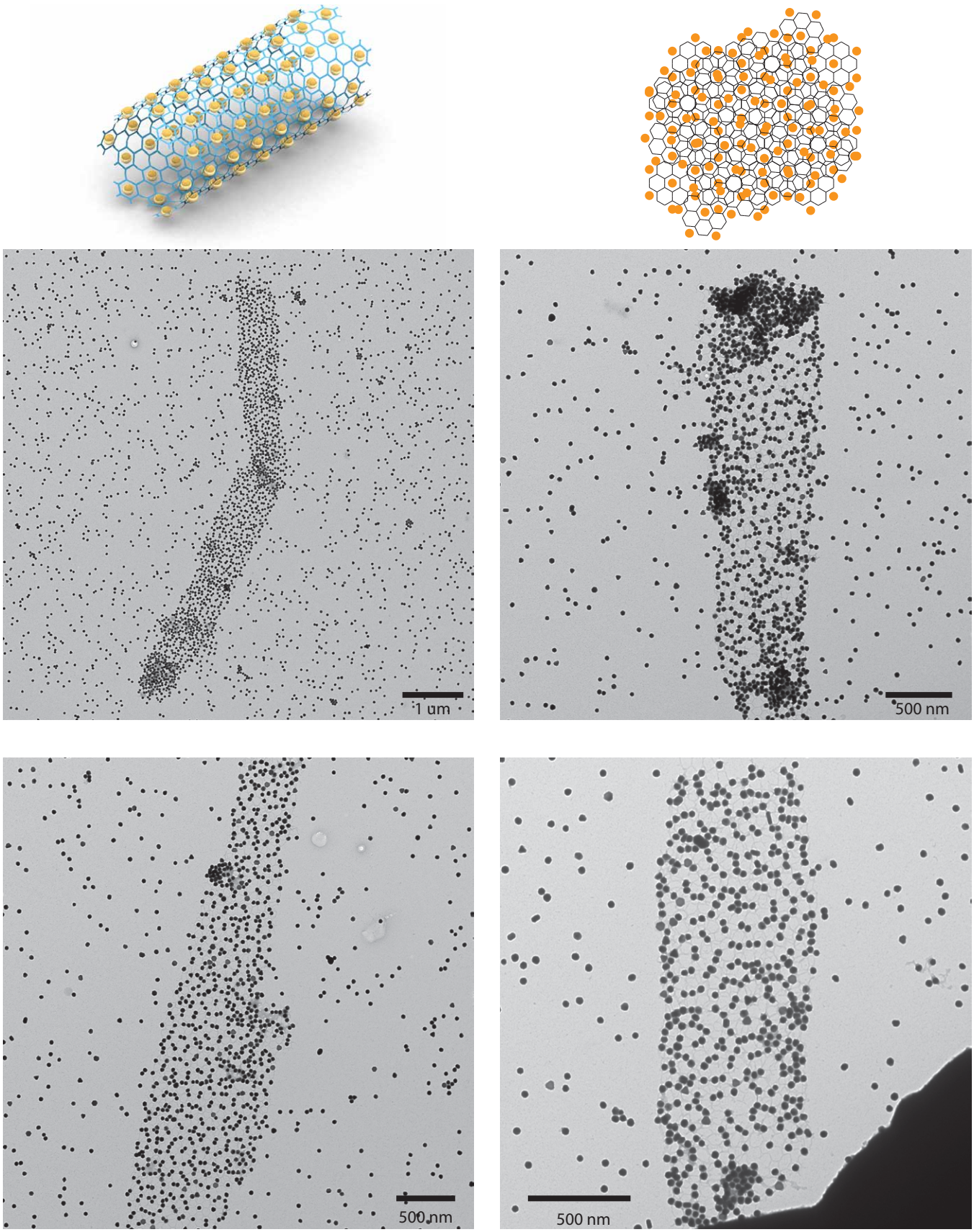

Fig. S29. TEM images of 30nm_Au_Tube_1 AuNP superlattice assembled on the 2×4 HT hexagonal origami tubes. A schematic model illustrating the overlapped pattern of AuNP superlattice matches well with the TEM observation.

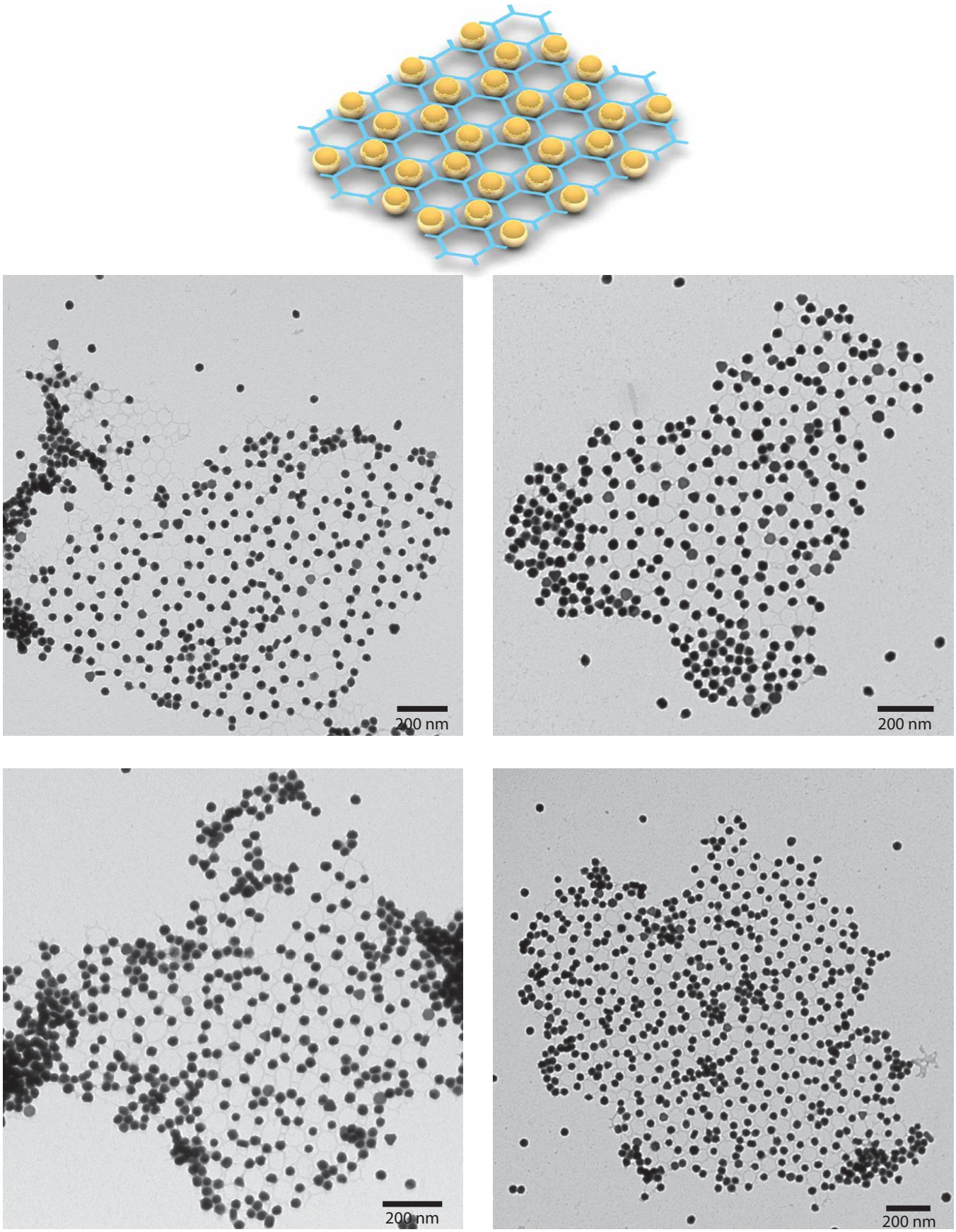

Fig. S30. TEM images of 30nm_Au_2D_2 AuNP superlattice assembled on the 2×4 HT hexagonal origami 2D lattices. A schematic model is presented on the top.

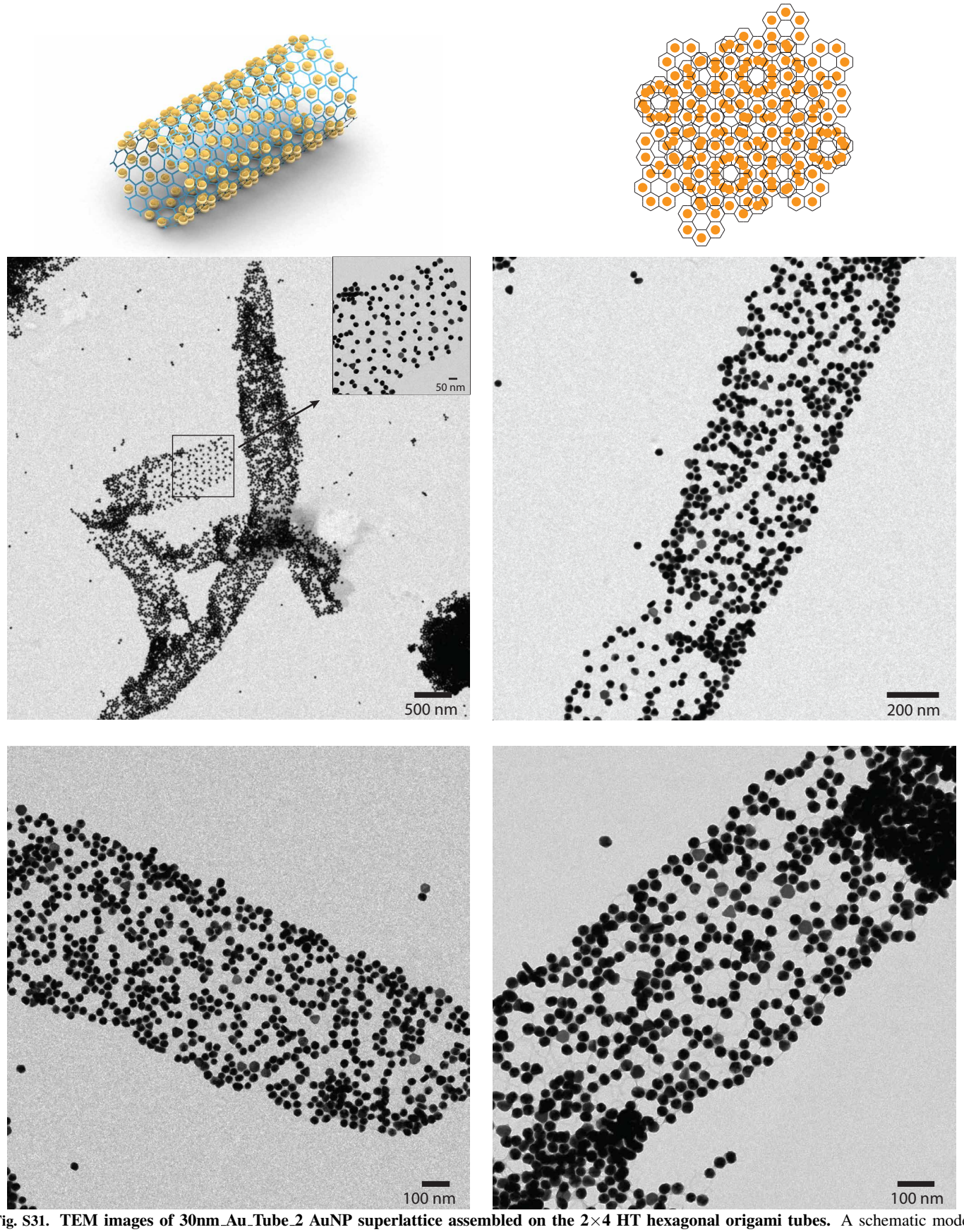

Fig. S31. TEM images of 30nm_Au_Tube_2 AuNP superlattice assembled on the 2×4 HT hexagonal origami tubes. A schematic model illustrating the overlapped pattern of AuNP superlattice is presented. Due to the large number of AuNPs and the deposition of AuNPs onto TEM grid surface, it is hard to make a direct match between the model and TEM images. Another significant evidence comes from the single-layer lattice at the broken end of the tube, as shown in the inset image.

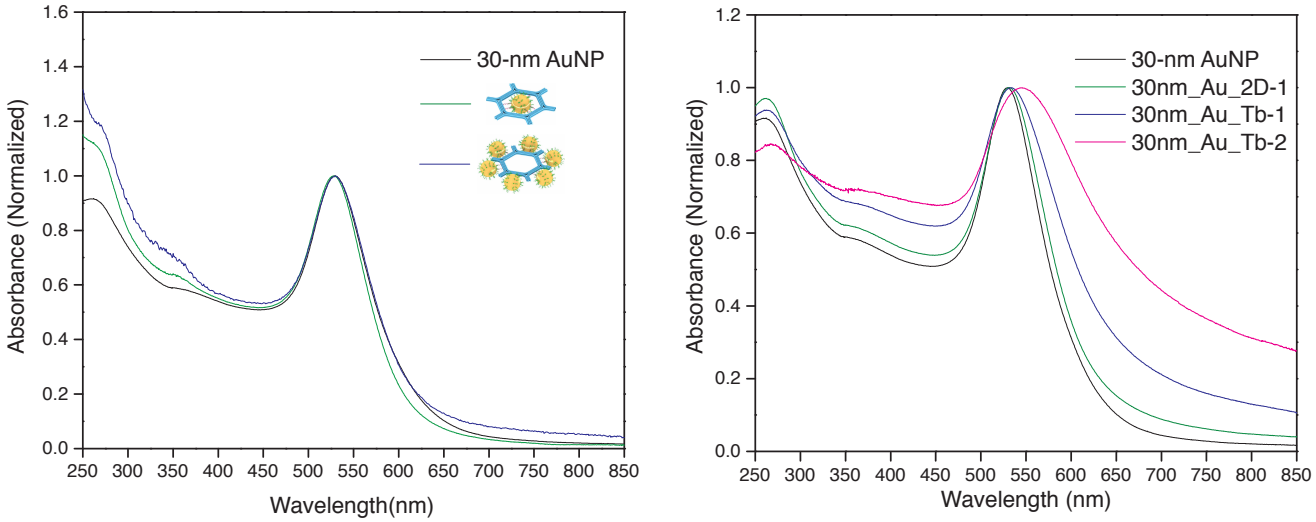

Fig. S32. UV-Vis absorption spectra of AuNP clusters and superlattices. No significant peak shift on the spectra are observed for AuNP clusters, comparing to discrete AuNPs, which indicates that inter-particle plasmonic coupling is not significant enough to induce higher electric resonance modes due to the relatively large spacing between AuNPs. Similar to 30nm_Au_2D_2, significant red-shift (16.5 nm) is observed for 30nm_Au_Tube_2 AuNP superlattice, suggesting there is strong plasmonic coupling between AuNPs due to close proximity.

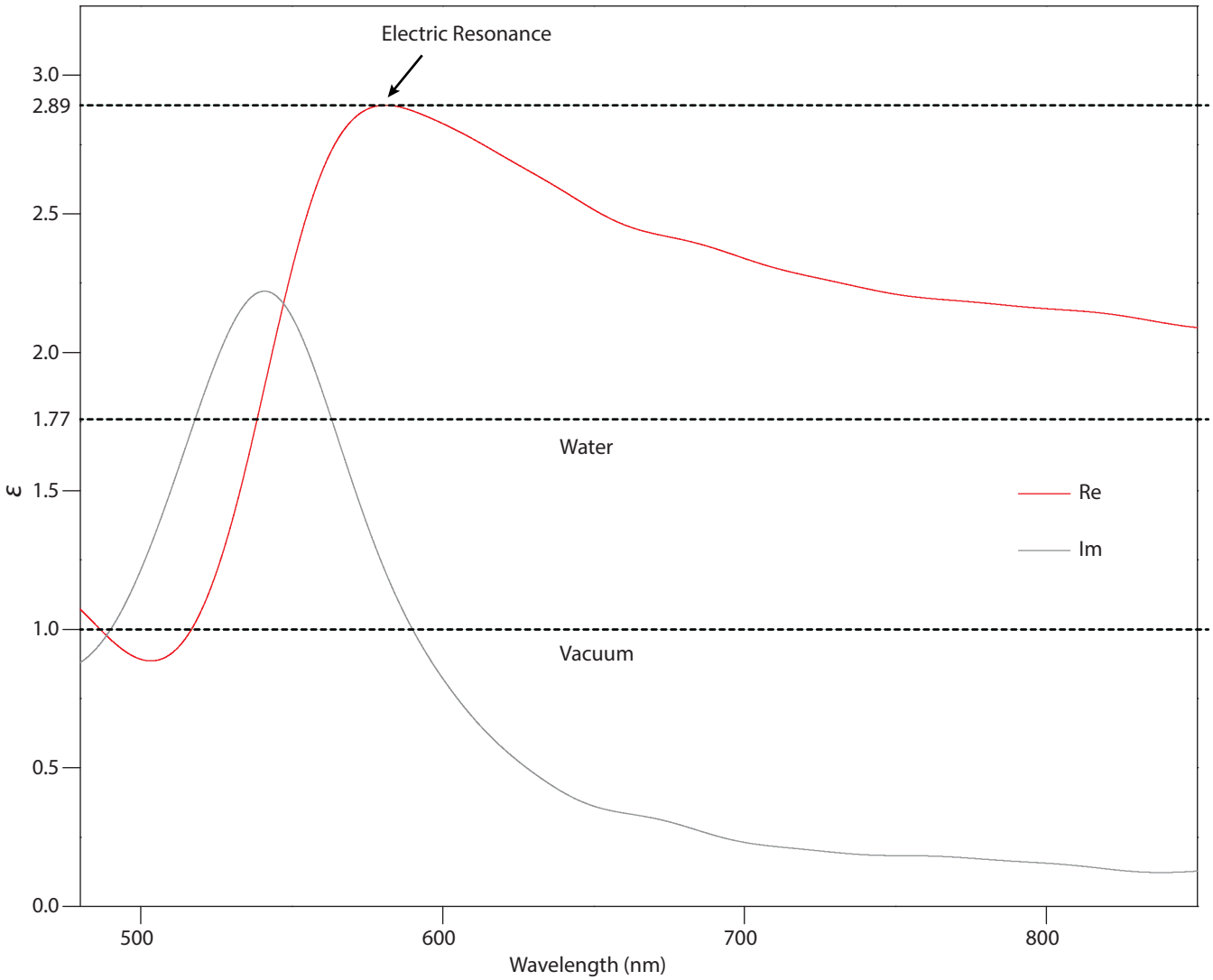

Fig. S33. Theoretically possible epsilon enhancement by dispersing the 30nm_Au_2D_2 AuNP superlattice in water. When the volume percent (%) of AuNP superlattice is 16.1, the effective epsilon, which is retrieved by using s-parameter extraction method based on effective medium theory, can be increased to from 1.77 to 2.89 at electric resonance.

S8 References

References

1. Douglas, S. M., Chou, J. J. & Shih, W. M. DNA-nanotube-induced alignment of membrane proteins for NMR structure determination. *Proc. Natl. Acad. Sci. U. S. A.* **104**, 6644–6648 (2007).
2. Castro, C. E. *et al.* A primer to scaffolded DNA origami. *Nature Methods* **8**, 221–229 (2011).
3. Kim, D. N., Kilchherr, F., Dietz, H. & Bathe, M. Quantitative prediction of 3D solution shape and flexibility of nucleic acid nanostructures. *Nucleic Acids Res.* **40**, 2862–2868 (2012).
4. Pan, K. *et al.* Lattice-free prediction of three-dimensional structure of programmed DNA assemblies. *Nat. Commun.* **5**, 5578 (2014).
5. Kim, M. *et al.* Deterministic assembly of metamolecules by atomic force microscope-enabled manipulation of ultra-smooth, super-spherical gold nanoparticles. *Opt. Express* **23**, 12766–12776 (2015).
6. Demarest, K., Huang, Z. & Plumb, R. An FDTD Near- to Far-Zone Transformation for Scatterers Buried in Stratified Grounds. *IEEE Trans. Antennas. Propag* **44**, 1150–1157 (1996).
7. Johnson, P. B. & Christy, R. W. Optical Constants of the Noble Metals. *Phys. Rev. B* **6**, 4370–4379 (1972).
8. Lee, S. Colloidal superlattices for unnaturally high-index metamaterials at broadband optical frequencies. *arXiv.org* 6854 (2015). 1507.06854.
9. Smith, D. R., Vier, D. C., Koschny, T. & Soukoulis, C. M. Electromagnetic parameter retrieval from inhomogeneous metamaterials. *Phys. Rev. E* **71**, 036617 (2005).